ELSEVIER

Contents lists available at ScienceDirect

Journal of Water Process Engineering

journal homepage: www.elsevier.com/locate/jwpe



PVP-assisted Ce-substituted UiO-66 nanoparticles: Engineering photocatalytic activity and adsorption for rhodamine B degradation

Maliheh Heravi ^{a,b}, Ali Ahmadpour ^{a,b,*}, Tahereh Rohani Bastami ^c, Mika Sillanpää ^{d,e,**}

- a Department of Chemical Engineering, Faculty of Engineering, Ferdowsi University of Mashhad, P.O. Box 91775-1111, Mashhad, Iran
- b Industrial Catalysts and Adsorbents and Environment Lab., Oil and Gas Research Institute, Ferdowsi University of Mashhad, Mashhad, Iran
- ^c Department of Chemical Engineering, Faculty of Advanced Technology, Quchan University of Technology, 94771-77870 Quchan, Iran
- ^d Institute of Research and Development, Duy Tan University, Da Nang, Viet Nam
- e School of Engineering & Technology, Duy Tan University, Da Nang, Viet Nam

ARTICLE INFO

Editor: Gamze Varank

Keywords: Metal-organic frameworks (MOFs) Adsorption Photocatalysis Visible light Rhodamine B

ABSTRACT

In this study, UiO-66(Ce) was synthesized via metal substitution using cerium salt and applied as a photocatalyst for Rhodamine B (RhB) degradation. The nano-sized crystals had a high surface area (1340 $\,\mathrm{m}^2/\mathrm{g}$), a pore diameter of 1.64 nm, and a band gap of 2.6 eV, showing strong activity under visible light. To enhance performance, polyvinylpyrrolidone (PVP) was used as a capping agent to control particle size and reduce aggregation. Optimization of the PVP-to-cerium ammonium nitrate (CAN) ratio led to a reduced band gap of 2.2 eV and particle size of 110 nm. Cycling tests confirmed good stability over three reuse cycles. Trapping and electron paramagnetic resonance (EPR) experiments identified photogenerated holes and superoxide radicals as the main active species. X-ray photoelectron spectroscopy (XPS) revealed a high Ce^{3+} concentration, suggesting oxygen vacancies contributed to the activity. Adsorption studies followed the Freundlich model ($\mathrm{R}^2=0.9921$), indicating multilayer adsorption. Kinetic modeling with the Langmuir–Hinshelwood approach yielded a rate constant of 0.0207 min^{-1} . Finally, a degradation efficiency of 92.9 \pm 0.4 % was achieved in 150 min using only 0.06 g/L of catalyst for 10 $\mathrm{mg/L}$ RhB solution which highlights the potential of PVP-assisted UiO-66(Ce) as a highly efficient and stable photocatalyst for wastewater treatment.

1. Introduction

Water contamination by organic dyes, such as Methyl Orange, Congo Red, and Rhodamine B (RhB), poses a severe environmental threat due to their persistence and toxic effects [1–3]. RhB is a synthetic, cationic dye widely used in various industries, including hydrology, biotechnology, and material processing, despite concerns regarding its potential carcinogenicity. It serves as a tracer dye in hydrological studies for monitoring water flow and contamination pathways due to its strong fluorescence properties [4]. In addition, RhB is frequently used as a fluorescent biological stain in microbiological applications and is widely applied in fluorescence microscopy, flow cytometry, and ELISA techniques in biotechnology [5]. Furthermore, it remains an essential colorant in the textile, leather, paper printing, paint, glass, and plastics industries, imparting bright pink and red hues to various products [1].

However, the environmental and health risks associated with RhB are significant. Due to its potential carcinogenicity, regulatory agencies in multiple countries have restricted or banned RhB usage in food products. Additionally, RhB is highly resistant to conventional wastewater treatment methods, leading to its long-term persistence in aquatic environments and posing toxic risks to aquatic organisms. This necessitates the development of efficient remediation strategies capable of completely degrading RhB and preventing its accumulation in ecosystems.

Photocatalysis under visible light has emerged as a promising approach for the degradation of organic pollutants like RhB (Table S1). Unlike traditional wastewater treatment methods, which often fail to achieve complete mineralization of dyes, visible-light-driven photocatalysis offers a sustainable and energy-efficient solution by utilizing a broader portion of the solar spectrum. This process facilitates the

^{*} Correspondence to: A. Ahmadpour, Department of Chemical Engineering, Faculty of Engineering, Ferdowsi University of Mashhad, P.O. Box 91775-1111, Mashhad, Iran.

^{**} Correspondence to: M. Sillanpää, Institute of Research and Development, Duy Tan University, Da Nang, Viet Nam.

E-mail addresses: ahmadpour@um.ac.ir (A. Ahmadpour), mikas@uj.ac.za, mikaetapiosillanpaa@duytan.edu.vn (M. Sillanpää).

generation of reactive species capable of degrading RhB into harmless end-products, enhancing both efficacy and feasibility for large-scale wastewater treatment applications.

Among advanced photocatalytic materials, metal-organic frameworks (MOFs) have gained significant attention due to their high surface area, tunable porosity, and customizable metal-ligand coordination structures [6]. MOFs are a class of porous crystalline materials synthesized through the self-assembly of metal clusters and organic ligands, enabling precise control over adsorption properties and catalytic activity [6]. Their intrinsic semiconducting properties allow them to function as next-generation photocatalysts, with metal nodes facilitating charge transfer and organic linkers enhancing light-harvesting efficiency [7]. Understanding the photocatalytic behavior of MOFs requires consideration of semiconductor-based photocatalysis principles. These principles govern the generation and activity of reactive species under light irradiation. Semiconductors have a specific band gap energy that allows them to absorb light. When a semiconductor absorbs photons with energy equal to or greater than the band gap, electrons are excited from the valence band (VB) to the conduction band (CB), leaving behind holes in the VB. This creates electron-hole pairs (e⁻/h⁺), which are the key active species in photocatalysis. The excited electrons in the conduction band and holes in the valence band can participate in redox reactions. Electrons (e⁻) can reduce electron acceptors (such as oxygen) to form reactive oxygen species like superoxide anions (\bullet O²⁻). Holes (h⁺) in the valence band can oxidize water or hydroxyl ions to form hydroxyl radicals (•OH). These reactive species are highly oxidative and can degrade organic pollutants through photocatalytic processes [8].

Within the MOF family, UiO-66, a zirconium-based structure, has been widely investigated due to its exceptional mechanical, chemical, and thermal stability [9]. It has been widely studied due to its high surface area and the potential for metal substitution and functionalization [10-13]. However, its photocatalytic activity is limited, particularly in the visible-light range (band gap is estimated to be 3.85 eV [14]). To address this limitation, metal substitution strategies have been explored to modify the electronic structure and bandgap energy of UiO-66, thereby enhancing its photocatalytic performance. Studies, such as those by Wu et al., have computationally demonstrated that replacing zirconium with cerium (Ce) significantly reduces the bandgap, making UiO-66(Ce) a more effective visible-light photocatalyst [15]. They demonstrated through scientific analysis that UiO-66(Ce) exhibits superior photocatalytic properties compared to other metal-substituted UiO-66 MOFs such as Zr, Hf, Th, Ti, and U. The incorporation of Ce⁴⁺ into the MOF framework introduces low-lying unoccupied 4f orbitals that enhance ligand-to-metal charge transfer (LMCT), facilitating rapid electron transfer and efficient separation of photogenerated charges. This process reduces electron-hole recombination and prolongs the lifetime of excited states, thereby improving photocatalytic performance. Furthermore, the presence of Ce3+ ions enhances the interactions between the catalyst surface and the reactant molecules, while the Ce⁴⁺/Ce³⁺ redox cycling enables dynamic electron transfer and further enhances photocatalytic activity. These combined electronic and redox properties make UiO-66(Ce) a very attractive photocatalyst for light-driven reactions and justify the choice of cerium in this study despite its higher material cost [16].

To further optimize morphology and photocatalytic performance, polyvinyl pyrrolidone (PVP) has been introduced as a stabilizing agent during UiO-66(Ce) synthesis. PVP is a biocompatible, water-soluble polymer widely used in nanoparticle synthesis to control particle size, prevent aggregation, and enhance surface properties [17]. It is commonly employed in pharmaceuticals, cosmetics, and detergents due to its non-toxic nature [18]. Inspired by these properties, we incorporated PVP as a morphology-regulating agent to refine the structure of UiO-66(Ce), ultimately enhancing its stability and photocatalytic efficiency. The addition of PVP during hydrothermal synthesis resulted in nanomaterials with improved dispersibility, reduced aggregation, and increased active surface sites for pollutant degradation. This enhanced

the overall photocatalytic activity of UiO-66(Ce), as demonstrated through the photodegradation of RhB under visible-light irradiation [19].

Beyond improving structural stability, PVP also plays a pivotal role in controlling nanoparticle morphology, which is essential for optimizing catalytic activity. Numerous studies have demonstrated that polymer-stabilized nanoparticles exhibit enhanced electrical, optical, and catalytic properties compared to their bulk counterparts [20]. PVP has been widely used in the synthesis of gold, silver, and rhodium nanoparticles, where it regulates crystal growth and prevents aggregation [21–23]. Despite its extensive use in metal-based nanostructures, limited research has explored its role in stabilizing MOF-based photocatalysts. In our study, PVP with a dual hydrophobic-hydrophilic nature serves two key roles in the synthesis environment: (1) it stabilizes nanoparticles and prevents aggregation through its hydrophobic regions (pyrrolidone group), and (2) it acts as a template to guide nucleation and control nanoparticle growth by encapsulation of MOF nanoparticles [17].

In this study, a novel UiO-66(Ce) MOF was successfully synthesized to enable efficient visible-light absorption, positioning it as a promising photocatalyst for environmental remediation and water treatment applications. A facile, PVP-assisted solvothermal method was developed, wherein PVP acted as a morphology-controlling and capping agent, effectively regulating particle growth, minimizing aggregation, and enhancing surface dispersion. This not only improved the availability of active sites for pollutant adsorption but also ensured uniform nanoscale crystallites. More importantly, the total substitution of Zr⁴⁺ with Ce⁴⁺ within the UiO-66 framework significantly narrowed the band gap, thereby improving visible-light harvesting and promoting better charge separation. This dual strategy—metal substitution to tune the band gap and PVP-assisted synthesis to control particle size and dispersion—represents a synergistic approach that markedly enhanced the photocatalytic degradation of Rhodamine B under visible-light irradiation. The results highlight the potential of rational framework engineering and surface modulation in designing efficient MOF-based photocatalysts.

2. Materials and methods

2.1. Chemical reagents

All chemicals were analytical grade and used directly without further purification. Cerium ammonium nitrate (CAN) (98 %, (NH $_4$) $_2$ Ce(NO $_3$) $_6$), 1,4,dicarboxylic acid (terephthalic acid (98 %, H $_2$ BDC), Polyvinylpyrrolidone (Mw = 40,000 g/mol), Rhodamine B (98 %), *N*,*N*-dimethylformamide (DMF) and acetone were purchased from Sigma-Aldrich. All solutions were prepared using ultrapure water prepared by Arium® Water Purification System.

2.2. Synthesis of UiO-66 (Ce) and PVP-assisted UiO-66 (Ce)

UiO-66(Ce) has been synthesized by a solvothermal method reported in Lammert $\it et.al$, literature with some modifications [24]. Typically, 35.4 mg (213 µmol) terephthalic acid as a linker was dissolved in 1.2 mL DMF and stirred for an hour (solution 1). After that, an aqueous solution of 0.5333 M CAN made in 400 µL deionized water (solution 2) was added to solution 1 using a Pyrex glass reaction tube. The glass reactor was put in an oil bath and heated while stirring for 20 min at 100 °C. Gradually, the uniform orange solution changed to a light-yellow suspension. After cooling at ambient temperature, the precipitates were collected from the mother liquor using a centrifuge and washed twice with DMF (2 mL) to remove the unreacted linker. Acetone (2 mL) was then used four times to remove DMF from the remaining solid. The resulting pale-yellow solid was dried in an oven for 6 h at 60 °C. Finally, the catalysts were collected in special sealed bottles and stored in a desiccator.

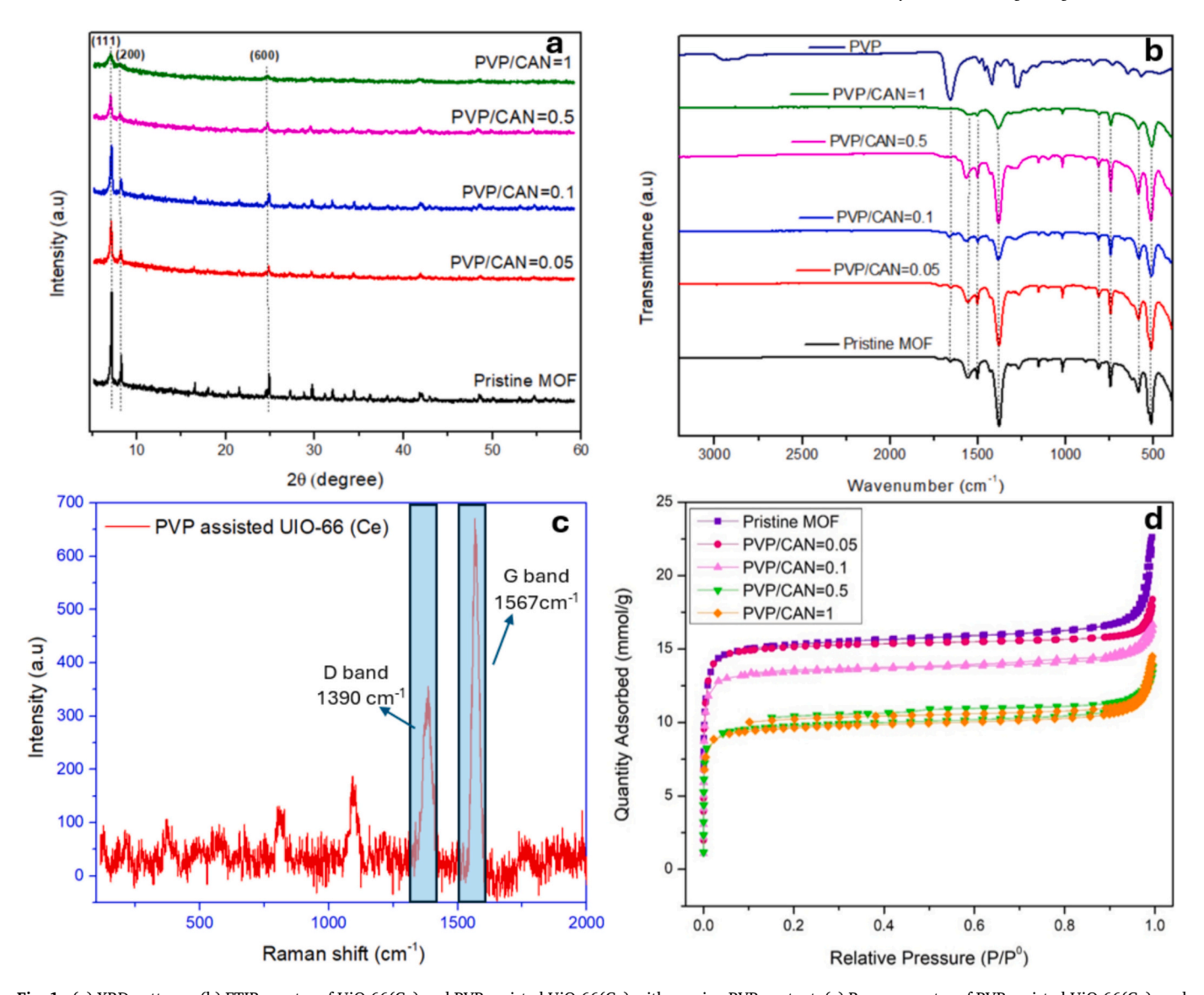


Fig. 1. (a) XRD patterns, (b) FTIR spectra of UiO-66(Ce) and PVP-assisted UiO-66(Ce) with varying PVP content, (c) Raman spectra of PVP-assisted UiO-66(Ce), and (d) Nitrogen adsorption—desorption isotherms of UiO-66(Ce) and PVP-assisted UiO-66(Ce) at varying PVP/CAN wt%.

PVP-assisted UiO-66 (Ce) has been prepared by the similar protocol of UiO-66 (Ce). The only difference is that PVP at various mass ratios of PVP/CAN 0.05, 0.1, 0.5, and 1 wt% was dissolved in the mentioned volume of deionized water before adding CAN. The resulting orange viscose mixture needs to be stirred for at least 1 h and then sonicated for about 30 min, making sure of complete dispersion.

2.3. Characterization of the catalysts

X-ray Diffraction (XRD, PANalytical X-ray diffractometer), X-Ray tube with Co anode (max 60 kV, 100 mA) with Co K α 1 radiation), Fourier transform infrared spectroscopy (FTIR, Bruker Vertex 70), Raman spectra (UniDRON model, Korea, equipped with 457, 532, and 785 nm excitation lasers), Brunauer, Emmett and Teller (BET, Tristar® II Plus) surface area, transmission electron microscopy (TEM, Hitachi H-7600), and scanning electron microscope (SEM, Hitachi, S-4800) were techniques used for the characterization of prepared nanophotocatalysts. Zeta potential was calculated by Zetasizer Nano ZS instrument. The concentration of pollutants was measured using a UV–vis spectrophotometer (Perkin Elmer Lambda 45, USA) in the wavelength range of 200–800 nm. For optical property analysis, the UV–vis diffuse reflectance spectra (DRS) were recorded using a separate UV–vis

spectrometer (Agilent Cary 5000) in the wavelength range of 250–800 nm, with a Spectralon standard as the reference. For photoluminescence (PL) analysis, the emission properties of the MOF samples were recorded using a PerkinElmer Luminescence Spectrometer LS 45 with a 246 nm excitation source. The surface composition and electronic states of elements in the photocatalyst were analyzed by X-ray photoelectron spectroscopy (XPS) using an ESCALAB 250Xi (Thermo Fisher Scientific) equipped with a monochromatic Al-K α (1486.6 eV) X-ray source. The concentration of dissolved Ce metal in the wastewater after photocatalytic tests was determined using inductively coupled plasma optical emission spectroscopy (ICP-OES) on an Agilent 5110. Electron paramagnetic resonance (EPR) analysis was performed using a CMS-8400 spectrometer from ADANI (Minsk, Belarus) to detect paramagnetic species. The spectral data were further analyzed using EasySpin 5.0 software.

2.4. Adsorption experiments

Rhodamine B was selected as a model molecule for dye adsorption. Typically, a stock solution of RhB with 100 mg/L concentration was prepared by dissolving a certain amount of dye powder in deionized water. All experimental solutions for the calibration curve drawing and

removal tests were prepared and diluted from the stock solution. For adsorption removal, 15 mg of the catalysts were added to 100 mL of RhB solution in different concentrations. The solutions were kept in darkness for a determined time, and 3 mL samples were collected at time intervals and filtered using 0.22 μm Minisart® syringe filters to collect solid particles of the catalysts. Absorption intensity of the filtered samples was analyzed by a UV–vis instrument at maximum peak of 554 nm. The reaction solutions were maintained homogeneously on a multiple plate magnetic stirrer at 500 rpm and room temperature. Adsorption study performed in different dye concentrations (20, 30, 50 and 70 mg/L), pH of the solution (the nature pH of RhB is 4.5 \pm 0.5) and temperature (35 and 45 °C) to obtain adsorption isotherm and kinetic parameters of different models.

2.5. Photocatalytic experiments

To investigate the photocatalytic performance of the samples, a 100 mL solution of RhB with 8 mg/L concentration at its natural pH was studied in a 150 mL beaker. 6 mg of catalysts were dispersed in the solution while stirring. Before exposure to light, the solution was stirred for 1 h in dark conditions to achieve thermodynamic equilibrium on the photocatalysts surface. Then, a 150 W VWR light emitting diode (LED) cold visible light source was used as the illumination source for photocatalytic experiments. The light was turned on, and at certain time intervals, 3 mL of the solution was sampled. The efficiency of the catalysts' degradation performance is measured using eq. (1) [25]:

$$\label{eq:definition} \text{Degradation efficiency } (q) = \frac{(C_0 - C)V}{m} \tag{1}$$

where C, C₀, V and m are the final concentration of RhB after photo degradation, RhB concentration at adsorption-desorption equilibrium, volume of the pollutant solution and the dosage of the catalyst, respectively. The error bars in plots represent the standard deviation obtained from three different trials at each condition.

In a trapping experiment using sodium oxalate (SO, 1 mmol/L), p-1,4-benzoquinone (BQ, 1 mmol/L), and methanol (1 mmol/L), the active species involved in the photocatalytic process were identified to capture superoxide radical (\bullet O²-), the hole (h⁺), and hydroxyl radical (\bullet OH) scavengers, respectively. The primary difference between this experiment and the photodegradation test was the addition of scavengers to the RhB solution before the catalyst was introduced [26,27].

3. Results and discussion

3.1. Mechanism of MOF formation

In a proper reaction media of MOF preparation, an organic linker and a metal salt are mostly involved in a solvothermal process based on solution crystallization. During the heating process, intermediate oligomers called secondary building units formed as the result of the reaction between metal-ligand and linkers [28]. Finally, the symmetric structure of MOF was formed by the repetition of those oligomers [28]. In this study, by the addition of CAN aqueous solution to H_2BDC dissolved in DMF, a reaction occurred between –COOH groups and metal ions. Indeed, the molecules of the linker and Ce^{4+} are coordinated to form UiO-66 (Ce). According to the results of the crystallography reported in Lammert et al. publication, the $[Ce_6O_4(OH)_4]^{12+}$ clusters in Ce-UiO-66-BDC are arranged in a cubic shape and twelve different BDC^{2-} molecules connect these clusters together to present the ultimate formula of $[Ce_6O_4(OH)_4(BDC)_6]$ [24]. A schematic illustration of the MOF formation process, as described in the text, is presented in Fig. S1.

3.2. Characterization

Fig. 1a shows the XRD analyses of the UiO-66 (Ce) and PVP-assisted

UiO-66 (Ce) nanostructures. Similar to the reported results in the literature [29,30]. The clear and sharp characteristic peaks of the pure UiO-66 (Ce) appeared at $2\Theta = 7.3^{\circ}$, 8.5° , and 25.3° with (111), (200) and (600) Miller indices, respectively, confirm that the material is crystalline with the same structure of UiO-66 [30,31]. Other weak diffraction peaks are located at $2\Theta = 17^{\circ}$ (400), 21.6° (511), 29.9° (711) and 43° (933) [30]. By comparing the XRD patterns of the present study to the previous works, the as-prepared MOF contains no impurities. In the XRD spectrum of the as-prepared samples, the position of the peaks has not changed in comparison to the pure structure, which can suggest that PVP is not incorporated into the MOF framework but only present in the surrounding environment. While there has been no obvious change in the spectra of the low-content PVP samples compared to pure MOF, peaks for the sample containing high amount of PVP (PVP/CAN = 1 wt %) have become weaker. This can be attributed to the amorphous nature of PVP. As an organic polymer, PVP does not contribute to sharp diffraction peaks, and its presence in higher amounts results in an increased fraction of non-diffracting material in the sample [32]. Additionally, excess PVP likely surrounds the MOF particles, reducing their relative crystallinity by preventing long-range structural ordering.

Fig. 1b shows FTIR spectroscopy of all as-prepared samples to study surface chemistry. The main absorption peaks can be seen at around 1654, 1557, 1504, 1395, 815, 745 and 668 cm⁻¹ which have a good accordance with results reported by [31]. The peaks at 815, 745 and 668 cm⁻¹ were linked to the vibration of O—H and C—H bands in the BDC ligand [33]. The most intense peak detected at 1385 cm⁻¹ was due to the O–C–O symmetric stretching, while the peak at 1550 cm⁻¹ represented the O–C–O asymmetric stretching in the carboxylate group of the BDC ligand [33]. The small peak at 1504 cm⁻¹ and 1654 referred to the vibration of C—C in a benzene ring and the stretching vibrations of C—O in the carboxylic acid presents in BDC, respectively [29,33]. Weaker FTIR peaks can be due to a dilution effect. If a high amount of PVP is present, it may dilute the MOF signals, reducing relative peak intensity. This does not mean the material is amorphous; rather, MOF signals are masked or less dominant.

Peak at 1430 cm⁻¹ in all PVP-assisted UiO-66 (Ce) samples assigned to the C—N stretching vibrations and the attachment of CH₂ groups present in the PVP pyrrole ring [29].

In the PVP FTIR spectrum, the sharpest peak appears at 1656 cm⁻¹, which is attributed to N—H bending vibrations, followed by another prominent peak at 1283 cm⁻¹ corresponding to C—N stretching vibrations [34,35]. This peak has shifted to 1267 cm⁻¹ in all PVP-assisted UiO-66 (Ce) samples which is due to the interaction of nitrogen atom of PVP and Ce—O bands in MOF [17]. Table S2 summarizes the observed FTIR bands for different samples, including pristine UiO-66(Ce), PVP-assisted UiO-66(Ce), and pure PVP, along with their corresponding vibrational assignments.

Raman spectroscopy was employed to investigate the structural composition of the PVP-assisted Ce-UiO-66 photocatalyst, with a particular focus on the distribution of carbonaceous forms (Fig. 1c). The spectrum obtained under 532 nm excitation exhibited two prominent peaks at approximately 1390 ${\rm cm}^{-1}$ (D band) and 1567 ${\rm cm}^{-1}$ (G band), which are characteristic of amorphous (disordered) and graphitic carbon, respectively. The D band arises from structural defects and disordered carbon atoms, while the G band corresponds to the E2g vibrational mode of ${\rm sp}^2$ -hybridized carbon atoms in graphitic domains [36].

The intensity ratio of the D to G bands (I_D/I_G) indicates a significant degree of disorder, which is attributed to residual PVP or its partial thermal decomposition during synthesis or drying. This interpretation is further supported by TGA analysis, which showed a reduction in thermal stability for PVP-modified samples.

Regarding N_2 -adsorption-desorption analysis (Fig. 1d), the adsorption isotherm, based on IUPAC classification, corresponds to the typical Type I, indicating the microporous nature of the samples (pores less than 2 nm in diameter) [37]. The key feature of a Type I isotherm is the steep uptake at low relative pressures (P/P₀ < 0.1), which indicates adsorption

Table 1BET analysis results of the photocatalysts.

Samples name	$S_{BET}^{a} (m^2/g)$	D _a b (nm)	V _t ^c (cm ³ /g)
Pristine UiO-66 (Ce)	1357.8	1.64	0.55
0.05 wt% PVP/CAN	1050.7	2.18	0.59
0.1 wt% PVP/CAN	905	2.29	0.51
0.5 wt% PVP/CAN	682	2.35	0.38
1 wt% PVP/CAN	673.5	2.37	0.38

in micropores. This steep rise suggests that the adsorption is dominated by micropore filling rather than multilayer adsorption. Additionally, the lack of a pronounced hysteresis loop or the small hysteresis observed when containing high PVP content, suggests that the pores are primarily microporous. If any hysteresis is present, it might be due to limited contribution of mesoporous behavior [37] or due to the adsorption-desorption process in narrow pores. Thus, the absence of a broad hysteresis loop supports the classification of the material as predominantly microporous.

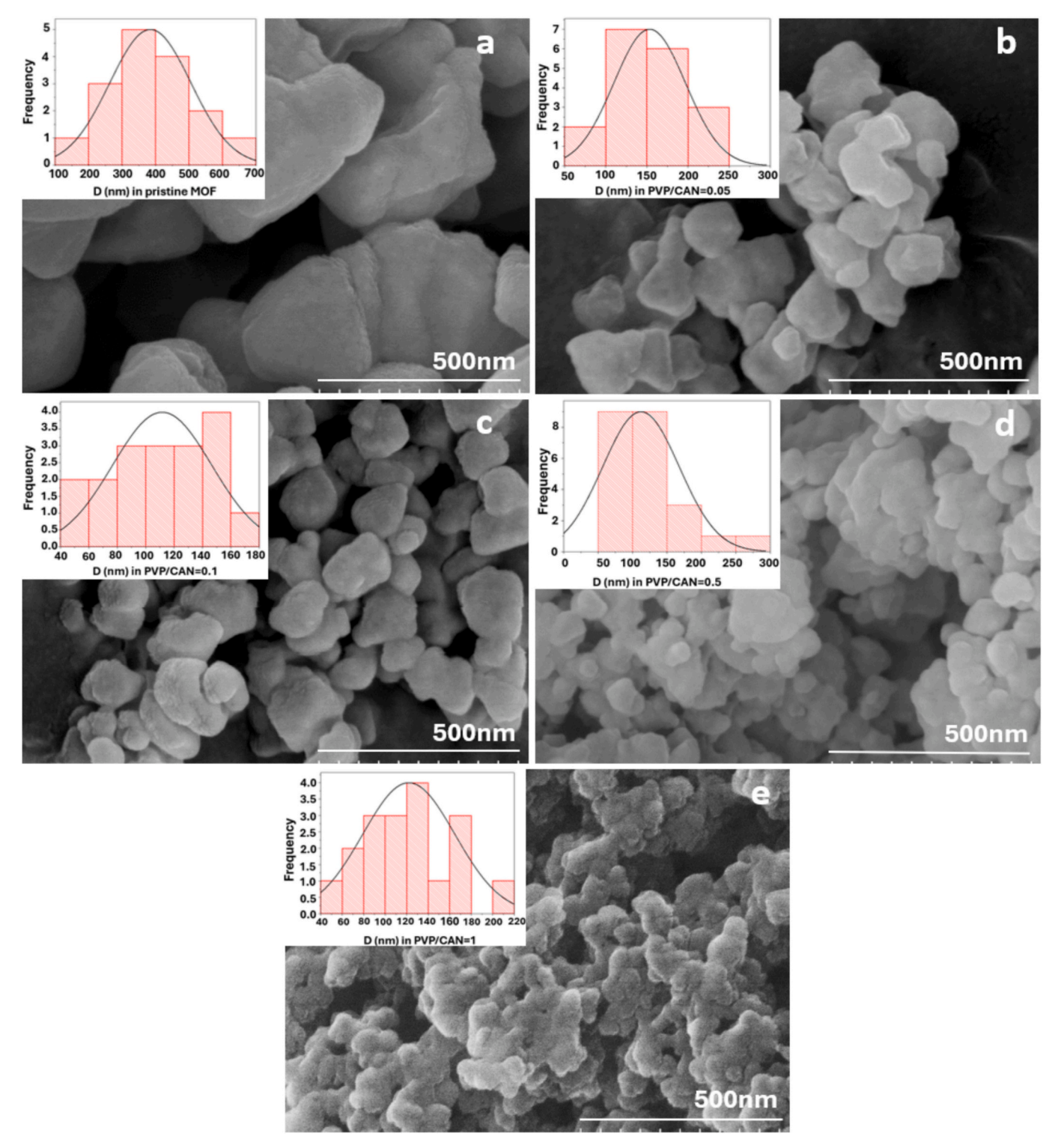


Fig. 2. SEM images of (a) UiO-66(Ce), and (b-e) PVP assisted UiO-66(Ce) with 0.05, 0.1, 0.5 and 1 wt%.

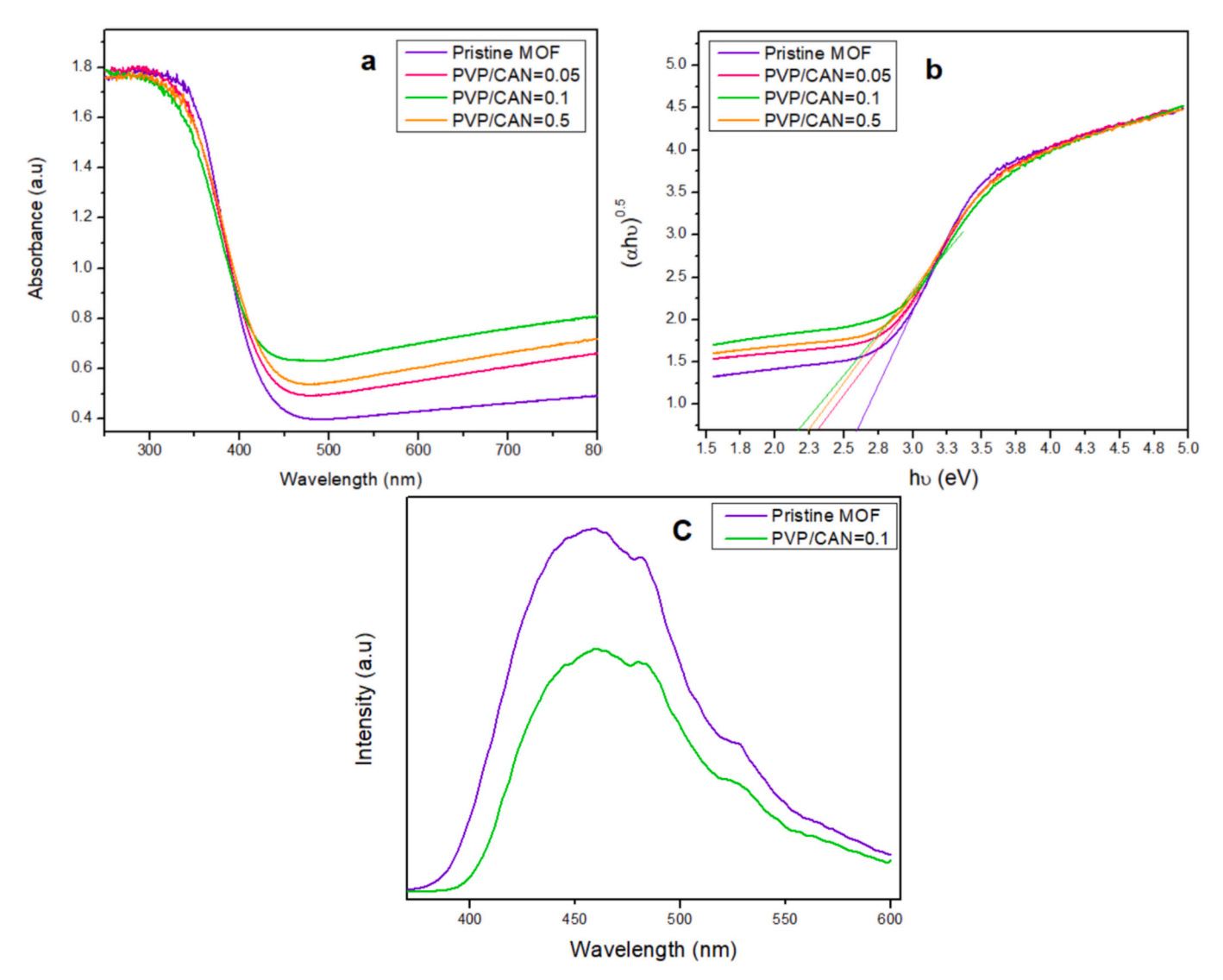


Fig. 3. (a) UV-vis diffusive reflectance spectra, (b) Estimation of bandgap energy for the fabricated samples, and (c) PL spectra.

The BET surface area, average pore diameter, and total volume of pores for as-prepared samples are reported in Table 1. The abundance of micropore in the structure of the UiO-66(Ce) nanoparticles can be the reason for relatively high BET surface area of as high as 1357 m²/g. When PVP is introduced in the in-situ synthesis, the BET surface area decreases progressively with increasing PVP content. This reduction is attributed to the structural influence of PVP on MOF formation, which may lead to denser packing of crystallites and partial occupation of micropores by residual organic molecules. Additionally, the average pore diameter increases as PVP selectively alters pore development, leaving larger mesopores accessible. The total pore volume also decreases, further confirming that PVP-modulated synthesis affects the overall porosity of the MOF structure. Unlike wet impregnation (where PVP physically coats the surface after synthesis), in-situ PVP synthesis integrates PVP into the reaction environment, affecting MOF growth. This means that PVP influences how pores develop during crystallization, rather than just blocking alreadyformed pores. In the presence of PVP, MOF crystal formation may be altered, leading to a denser, less porous structure. Some micropores may not fully develop, resulting in a lower BET surface area despite the reduction in particle size. Indeed, PVP may act as a soft template, leaving residues in pores; some PVP molecules might remain trapped within the MOF structure after synthesis, partially occupying micropores. Even after washing/drying, residual organic content can reduce pore accessibility for N2 adsorption [38].

The SEM images of pristine UiO-66(Ce) and PVP-assisted UiO-66(Ce) at varying PVP/CAN weight percentages (Fig. 2a-e) reveal significant changes in particle morphology. All SEM images were taken at a magnification of 500 nm, ensuring a consistent comparison of particle size variations across different synthesis conditions. In the absence of PVP, the particles appear larger with an average size reaching approximately 400 nm (Fig. 2a). With the addition of PVP as a capping agent, a gradual reduction in particle size is observed, indicating its role in controlling crystal growth. However, at higher PVP concentrations (PVP/CAN \geq 0.5 wt%), excessive polymer content leads to increased particle agglomeration, likely due to enhanced interparticle interactions. Image analysis using ImageJ software further confirms these trends, showing that the sample with 0.1 wt% PVP/CAN exhibits the most uniform particle size distribution, ranging from 80 nm to 140 nm (Fig. 2c), suggesting an optimal balance between size control and dispersion.

Additionally, the SEM image reveals that UiO-66(Ce) nanoparticles exhibit a predominantly rounded and polyhedral morphology, with particles showing irregular edges and a tendency to agglomerate [24]. The degree of clustering increases with higher PVP concentrations. Additionally, the rough particle surfaces suggest possible porosity, which may contribute to enhanced adsorption properties. These findings confirm that PVP plays a significant role in modifying both particle size and morphology, with excess amounts leading to clustering, negatively impacting particle uniformity and increased aggregation.

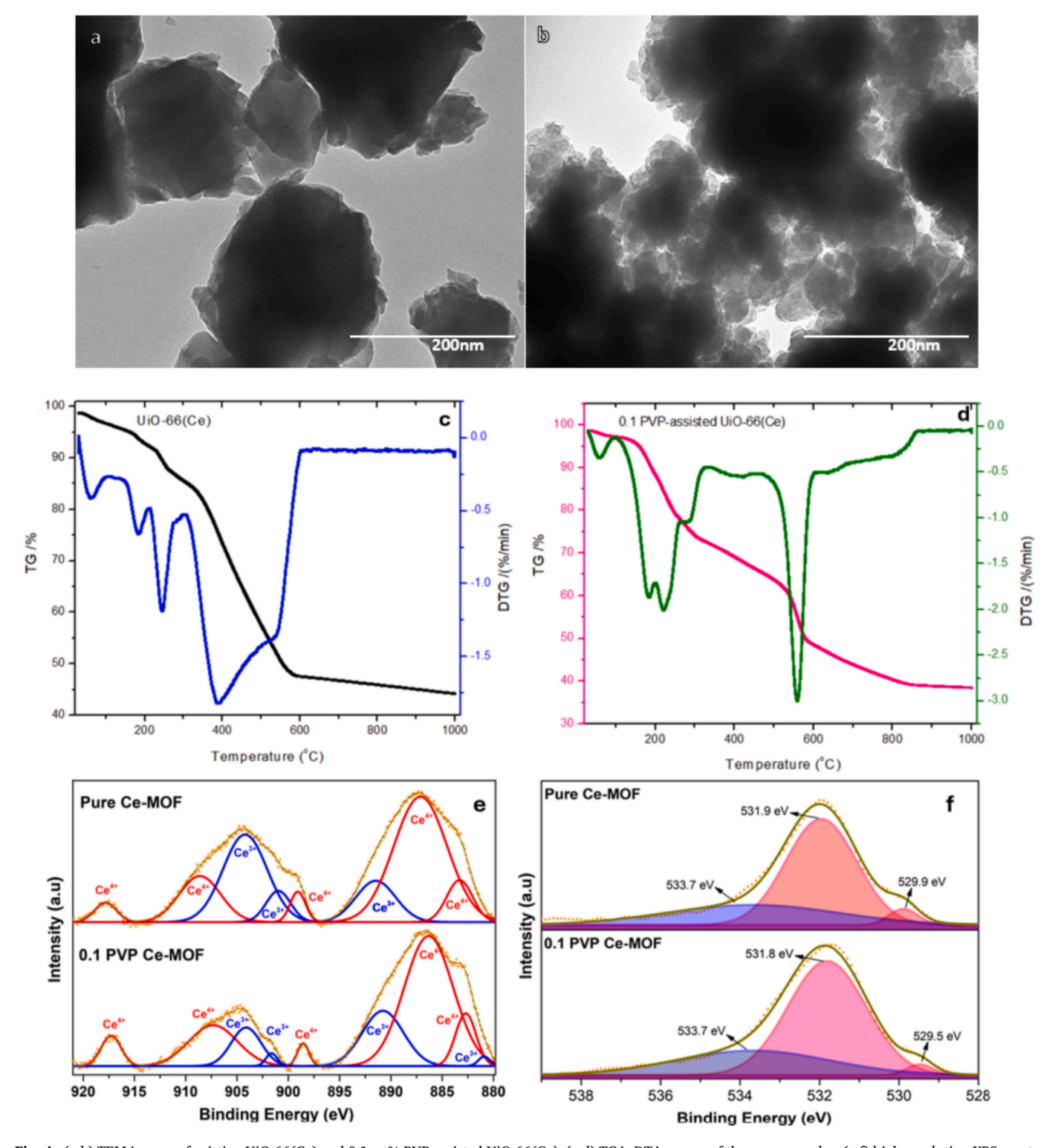


Fig. 4. (a,b) TEM images of pristine UiO-66(Ce) and 0.1 wt% PVP-assisted UiO-66(Ce); (c,d) TGA-DTA curves of the same samples; (e,f) high-resolution XPS spectra (Ce 3d and 0.1 s, respectively), upper spectrum corresponds to pristine UiO-66(Ce) and the lower spectrum to 0.1 wt% PVP-assisted UiO-66(Ce).

EDS analysis is a useful tool to investigate the elemental composition of the samples. As is obvious in the figures, from Fig. S2a to e, the carbon percentage increases, while Ce amount is getting less by adding more PVP to the structure. The increased carbon content in sample (b) compared to (a) can be attributed to the PVP addition, as PVP is an organic polymer rich in carbon. The higher oxygen content in sample (b) is consistent with the presence of PVP, which contains oxygen atoms. Carbon content is also due to the organic ligands involved. Sample (b)

has a higher oxygen content than sample (a), suggesting a higher degree of oxidation or more oxygen-containing functional groups. The lower cerium content in sample (b) could be due to PVP's capping effect, reducing the relative surface exposure of cerium for EDS detection. This trend is continued in other figures (Fig. S2c-e).

The optical absorption characteristics of a semiconductor directly influence its photocatalytic performance. To assess this, the light absorption capacity of the as-synthesized samples was measured using

UV-vis diffuse reflectance spectra (DRS), as shown in Fig. 3a. The S-shaped spectra (Fig. 3b) indicates that the visible-light absorption is due to band-gap transitions rather than impurity-induced transitions [17].

The band gap energy of a semiconductor is crucial in determining its photocatalytic degradation efficiency. Using the Tauc approach, the band gap energy (E_g) can be estimated by plotting ($\alpha h \nu$)^{n/2} against photon energy ($h \nu$), where α is the absorption coefficient, h is Planck's constant, ν is the frequency of light, and n depends on the nature of the optical transition (with n=1 for direct transitions and n=4 for indirect transitions) [17]. The intercept of the tangent to the X-axis in this plot provides the band gap energy for the synthesized photocatalysts.

The measured band gap energies were 2.6 eV for the pristine UiO-66 (Ce), 2.36 eV for 0.05 wt% PVP/CAN, 2.2 eV for 0.1 wt% PVP/CAN, and 2.3 eV for 0.5 wt% PVP/CAN. The smallest band gap was observed for the 0.1 wt% PVP/CAN sample at 2.2 eV, indicating that this material can be more easily excited under visible light, which would lead to the generation of more electron-hole pairs and potentially higher photocatalytic efficiency in degrading Rhodamine B. The reduction in band gap values compared to the pristine UiO-66(Ce) suggests that the incorporation of PVP/CAN into the MOF structure affects the electronic properties of the material. The slight increase in the band gap for the 0.5

wt% PVP/CAN sample may be due to variations in the interaction between the PVP and the CAN, potentially affecting the distribution of electronic states within the material. These results suggest that the energy band structure and optical properties of the UiO-66(Ce) assisted PVP samples are significantly influenced by the presence and ratio of PVP/CAN, which in turn affects their photocatalytic activity.

The photoinduced charge separation efficiency of UiO-66(Ce) and PVP-assisted UiO-66(Ce) was evaluated using photoluminescence (PL) emission spectroscopy. Broad PL peaks were observed in the range of 430–500 nm (Fig. 3c). It is well known that lower PL intensity corresponds to a higher separation rate of photoinduced charge carriers [33]. In this context, the PL intensity of PVP-assisted UiO-66(Ce) was significantly lower than that of pristine UiO-66(Ce), which is consistent with its improved catalytic performance. In particular, the pristine MOF exhibited a strong emission peak centered around 460 nm, indicating a high recombination rate of charge carriers. In contrast, the PVP/CAN = 0.1 sample showed pronounced PL quenching, suggesting more efficient electron–hole separation. This reduction in PL emission implies that the incorporation of PVP and ceric ammonium nitrate (CAN) improved the charge transfer dynamics and consequently enhanced the photocatalytic activity.

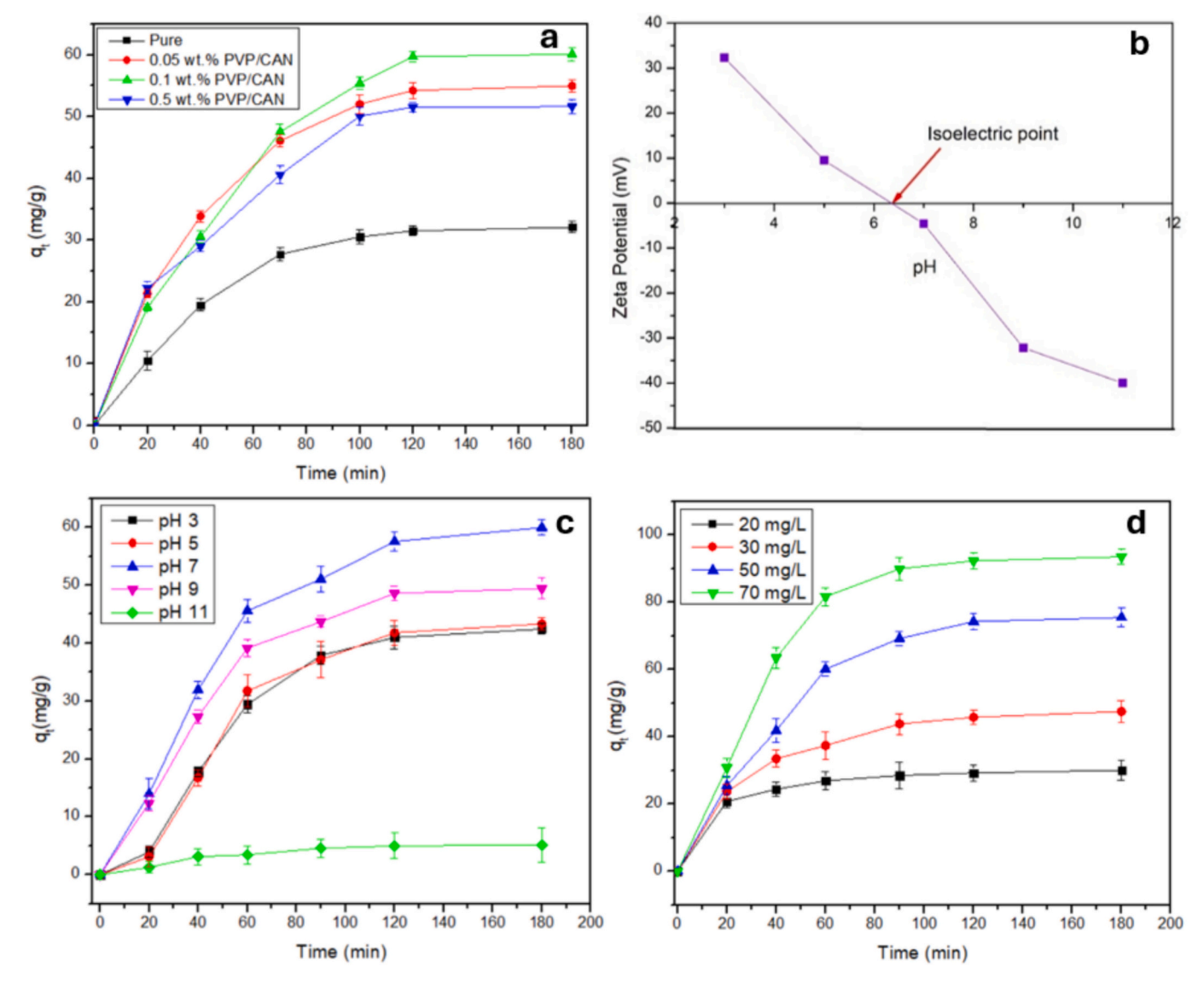


Fig. 5. (a) Effect of varying PVP content on RhB (20 mg/L) adsorption performance at pH = 4.5; (b) Zeta potential of 0.1 wt% PVP-assisted UiO-66(Ce); (c) Effect of initial pH of RhB solution on adsorption capacity of 0.1 wt% PVP-assisted UiO-66(Ce); (d) Effect of initial RhB concentration on adsorption capacity of 0.1 wt% PVP-assisted UiO-66(Ce) at pH = 7. Experimental conditions for (a,c, and d): Volume = 100 mL, Catalyst dosage = 20 mg, Temperature = 25 °C.

Based on previous characterization results, the sample containing 0.1 wt% PVP/CAN is potentially the optimum photocatalyst. Accordingly, we conducted TEM (Fig. 4a,b), TGA (Fig. 4c,d), and XPS (Fig. 4e,f) to elucidate the morphology, thermal behavior, and surface chemistry of the 0.1 wt% PVP/CAN sample, benchmarked against pristine UiO-66 (Ce). The first TEM image (Fig. 4a) depicts the pristine MOF synthesized without the addition of any capping agent. The particles exhibit a relatively large particle size (>200 nm) and a tendency to form larger aggregates, indicative of uncontrolled crystal growth. Conversely, the second TEM image (Fig. 4b) shows the MOF synthesized in the presence of PVP. The addition of PVP resulted in a marked reduction in particle size (< 100 nm) and a more uniform distribution which was also evident from the SEM analysis (Fig. 2c).

Thermogravimetric analysis (TGA) and derivative thermogravimetric (DTG) plots (Fig. 4c and 4d) of pristine UiO-66(Ce) and 0.1 PVP-assisted UiO-66(Ce) reveal distinct thermal decomposition behaviors, highlighting the influence of PVP on the thermal stability of the material.

For the pristine UiO-66(Ce), an initial mass loss of approximately 2.7 % was observed below $100\,^{\circ}$ C, which was attributed to the desorption of physically adsorbed moisture and volatile components. A secondary weight loss (~6.8 %) occurred between 167 °C and 229 °C, which was associated with the release of residual solvent molecules (e.g., DMF) trapped in the pores of the MOF. The major decomposition step appeared between 350 °C and 570 °C, accounting for approximately 38 % of the mass loss, which corresponds to the degradation of the organic linker (terephthalic acid) and the collapse of the UiO-66 framework. The residual mass at a temperature of about $1000\,^{\circ}$ C was 44 %, which is consistent with the formation of stable cerium oxide (CeO₂).

In contrast, PVP-assisted UiO-66(Ce) showed a slightly higher initial weight loss (\sim 3 %) below 100 °C, which is likely due to the hydrophilic nature of PVP that enhances moisture adsorption. Additional weight loss steps were observed between 158 $^{\circ}\text{C}$ and 244 $^{\circ}\text{C}$ and also between 300 $^{\circ}\text{C}$ and 575 $^{\circ}\text{C}.$ The more prominent DTG peaks in this sample indicate that PVP degradation occurs alongside the decomposition of the MOF framework. The total weight loss up to 834 °C was approximately 61 %, which is higher than the pristine material, primarily due to the thermal decomposition of PVP. The final residual mass at 999 °C was 38 % lower than the pristine sample, further confirming the influence of PVP on thermal stability. Although this reduction in thermal stability may limit its use in high-temperature applications such as gas-phase catalysis or pyrolysis-related processes, it is acceptable for lowtemperature operations, including aqueous-phase photocatalysis, adsorption, and removal of pollutants at ambient-temperatures. Furthermore, the PVP incorporation offers structural advantages such as improved particle dispersion and better active site accessibility, which can enhance catalytic performance in these low-temperature applications.

The XPS analysis was employed to understand the valence states of Ce in the MOF structure of pristine UiO-66 (Ce) and 0.1 wt% PVPassisted UiO-66 (Ce). Fig. 4e shows the Gaussian-fitted Ce 3d spectra which exhibits multiple splitting of peaks which can be ascribed to spinorbit components of $3d_{3/2}$ and $3d_{5/2}$ [39,40]. The XPS peaks at 917.3 eV, 907.3 eV, 898.5 eV, 886.3 eV and 882.6 eV in 0.1 wt% PVP-assisted UiO-66 (Ce) marked in red color are assigned to Ce⁴⁺, whereas the peaks at 904.2 eV, 901.6 eV, 890.9 eV and 880.9 eV marked in blue color are due to Ce³⁺. Similar peaks are also observed in UiO-66 (Ce) which showed peaks at 917.8 eV, 908.5 eV, 899.1 eV, 887.1 eV and 883.3 eV which is ascribed to Ce⁴⁺ and the peaks at 904. eV, 901.1 eV and 891.5 eV are assigned to Ce^{3+} [41,42]. However, the peak intensities at 904.1 eV and 901.1 eV for Ce³⁺ are significantly higher in pure UiO-66 (Ce) compared to 0.1 wt% PVP-assisted UiO-66 (Ce). Nevertheless, there is a coexistence of both Ce³⁺ and Ce⁴⁺ in both the samples. The presence of significant amount of Ce3+ state indicates that there are more nonstoichiometric CeO2 formed in the material which could lead to increased oxygen vacancies and can positively impact the activity of the

material [41].

The O1s spectra of both pristine UiO-66 (Ce) and 0.1 wt% PVP-UiO-66 (Ce) in Fig. 4f showed three major peaks. These peaks are attributed to surface chemisorbed oxygen (\sim 533.7 eV), surface-active oxygen (\sim 531.8 eV) and lattice oxygen (\sim 529.5 eV) [43]. The presence of very high amount of surface-active oxygen (\sim 531.8 eV) in both pristine UiO-66 (Ce) and 0.1 wt% PVP-assisted UiO-66 (Ce) indicates the presence of higher oxygen vacancies in the catalysts which can enhance the catalytic activity of the material [39].

3.3. Adsorption experiments in darkness

3.3.1. Effect of contact time

Results obtained from characterization proved that mass ratio 0.1 wt % PVP-assisted UiO-66(Ce) suggests more separated particles with smaller particle size and diameter and higher surface area. However, the experimental priority of this photocatalyst over other ones needs to be investigated. Therefore, Fig. 5a displays adsorption performance of all as-prepared nanostructures. It should be mentioned that 1 wt% PVP-assisted UiO-66(Ce) was excluded from the options due to its agglomerated particles, low surface area as low as 0.5 wt% PVP-assisted UiO-66 (Ce), and challenges encountered during precursor preparation.

It is obvious that PVP has influenced the process of adsorption. Although the slopes are similar in the first 20 min, 0.1 wt% PVP-assisted UiO-66 (Ce) shows higher adsorption capacity (qt) after 1 h. Therefore, it was selected for the following experiments. To further investigate the effect of parameters on adsorption performance of 0.1 wt% PVP-assisted UiO-66 (Ce), pH of the solution, and RhB concentration were studied.

3.3.2. Effect of solution pH

The pH of the solution is a critical factor in determining the adsorption of Rhodamine B (RhB) on the catalyst surface due to potential electrostatic interactions. Before conducting adsorption experiments, it is essential to adjust the pH of the solution to specific values, as the surface charge of the nanoparticles (zeta potential, Zpnt) varies with pH. The natural pH of RhB dissolved in distilled water is approximately 4.5 ± 0.5 , as the carboxyl group remains in its deprotonated state [44]. To understand the effect of pH on adsorption, experiments were carried out at different pH levels (3, 5, 7, 9, and 11) by adjusting the solution with 0.1 M NaOH or HCl. The zeta potential of the particles was measured across these pH values, with the procedure involving dispersing 1 mg of the nanoparticles in 10 mL of distilled water, followed by sonication for 10 min before injection into the zeta potential measurement cell. According to literature, RhB exists in its cationic form (RhB⁺) in acidic conditions [45]. According to Fig. 5b, at pH values lower than the point of zero charge (pzc), which is around pH 6.35 for the catalyst, the surface charge is positive, leading to electrostatic repulsion between the positively charged RhB and the catalyst surface. This repulsion reduces the adsorption efficiency, as observed at pH 3 and 5, where the adsorption capacities are similar and lower than at higher pH levels. As the pH increases beyond the pK_a of RhB (3.7), RhB starts to deprotonate, forming zwitter ions, which possess both positive and negative charges [46]. Regarding Fig. 5c, the highest adsorption was observed at pH 7, where the catalyst surface is negatively charged, and the RhB molecules in the solution are still partially protonated, allowing effective electrostatic attraction. However, as the pH approaches 10, RhB becomes fully deprotonated, resulting in a higher concentration of negatively charged species [47]. Concurrently, the catalyst surface also becomes increasingly negatively charged due to the high concentration of OH ions [48]. This leads to significant electrostatic repulsion between the negatively charged RhB species and the catalyst surface, drastically reducing adsorption. At pH 11, this repulsion is so strong that no adsorption of RhB occurs on the catalyst surface.

3.3.3. Effect of initial dye concentration

To evaluate the effect of initial dye concentration on the adsorption

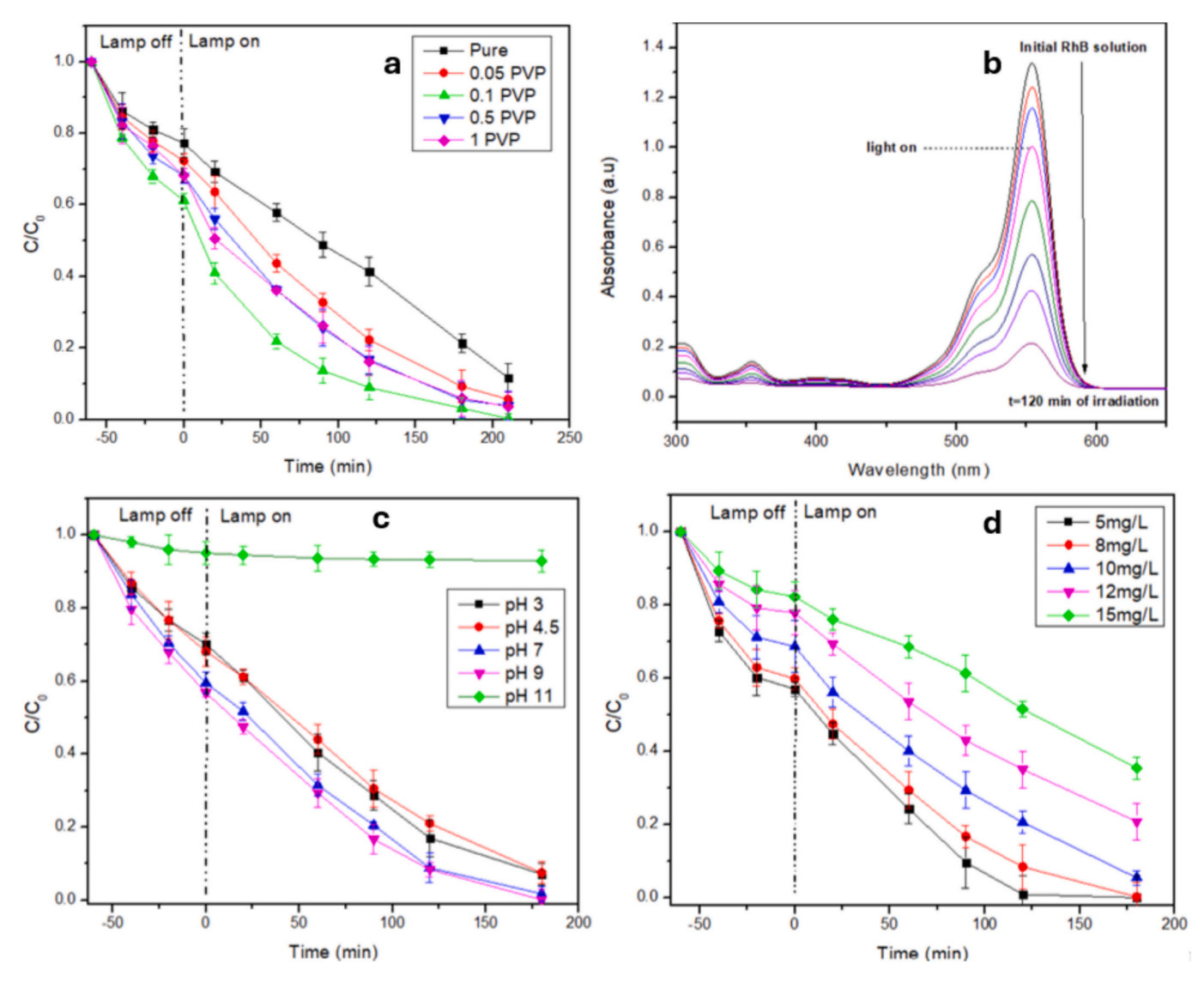


Fig. 6. (a) Effect of contact time on RhB photocatalytic efficiency (8 mg/L) over PVP-assisted UiO-66(Ce) with varying PVP/CAN wt% at pH = 4.5; (b) Photodegraded RhB solutions ($C_i = 8$ mg/L) and their corresponding visible spectra over 0.1 PVP-assisted UiO-66(Ce) at pH = 4.5; (c) Effect of solution pH on RhB photocatalytic efficiency ($C_i = 8$ mg/L) over 0.1 wt% PVP-assisted UiO-66(Ce); (d) Effect of initial RhB concentration on photocatalytic removal efficiency over 0.1 wt% PVP-assisted UiO-66(Ce) at pH = 7. Experimental conditions (unless otherwise stated): Volume = 100 mL, catalyst dosage = 6 mg, temperature = 25 °C.

capacity, the experiments were conducted with varying initial concentrations of the dye (20, 30, 50, and 70 mg/L), and the adsorption capacity (qt) was measured over time, as shown in the Fig. 5d. The results indicate that the adsorption capacity increased with the initial concentration of the dye as time progressed. At lower concentrations (20 mg/L and 30 mg/L), the adsorption reached equilibrium more slowly, with qe values of approximately 30.2 \pm 1.1 mg/g and 46.8 \pm 1.5 mg/g, respectively. As the initial dye concentration increased to 50 mg/L and 70 mg/L, the adsorption capacity significantly improved, reaching higher qe values of around 75.3 \pm 2.0 mg/g and 93.1 \pm 2.6 mg/g, respectively.

This trend suggests that higher initial dye concentrations provide a greater driving force for mass transfer, resulting in more dye molecules being adsorbed onto the catalyst surface [49]. The faster approach to equilibrium at higher concentrations also indicates a higher availability of active sites on the catalyst surface, leading to increased adsorption efficiency [49]. However, as the dye concentration increases, the active sites on the catalyst surface become more saturated, leading to a quicker approach to equilibrium. This saturation effect at higher concentrations results in a higher adsorption capacity, but it also means that the catalyst

surface becomes fully covered by dye molecules more rapidly [50].

3.4. Photocatalysis test

3.4.1. Effect of contact time

Before the visible light was turned on, all samples were subjected to a dark adsorption phase to ensure equilibrium was reached. Once the lamp was activated, the photocatalytic degradation of Rhodamine B was monitored over time. The initial phase of the experiment, with the lamp off, confirms that the decrease in concentration during this period was due to adsorption rather than photocatalytic activity. Once the lamp was turned on, a more significant reduction in Rhodamine B concentration is observed due to photocatalysis. As shown in the Fig. 6a, the degradation of Rhodamine B using the 0.1 wt% PVP/CAN sample was notably efficient. After 180 min of visible light exposure, the concentration of Rhodamine B (C/Co) for the 0.1 wt% PVP/CAN sample decreased to approximately 0.05, indicating that nearly 95 % of the dye was degraded. In contrast, the pristine UiO-66(Ce) achieved only $\sim\!60$ % degradation (C/Co) \approx 0.4) under the same conditions. The time-dependent visible spectra for degradation of RhB over 0.1 PVP-

assisted UiO-66(Ce) are also presented in Fig. 6b.

3.4.2. Effect of pH on degradation

As seen in Fig. 6c. With an increase in pH, the oxidizing potential of semiconductor-generated holes was enhanced. This facilitates the oxidation of hydroxide ions, leading to the formation of hydroxyl radicals. In more alkaline conditions, hydroxide ions are more easily converted into hydroxyl radicals on the catalyst surface. As a result, the photocatalytic degradation of Rhodamine B improves with increasing pH [51,52]. Additionally, under basic pH conditions, the formation of hydroxyl radicals (•OH) may enhance the degradation of RhB and its intermediates, promoting the reaction through an •OH radical oxidation mechanism. However, as the pH exceeds 10, the efficiency of RhB degradation decreased due to the strong electrostatic repulsion and the loss of RhB protonation, leading to minimal interaction with the negatively charged catalyst surface.

3.4.3. Effect of initial dye concentration

The effect of initial RhB concentration on photocatalytic removal was investigated, and the observed trend follows a logical pattern (Fig. 6d). At lower initial concentrations (5 mg/L and 8 mg/L), the degradation rate was significantly higher, with nearly complete removal within the reaction time. However, as the concentration increased (10, 12, and 15 mg/L), the degradation rate slowed down, and the removal efficiency decreased. This can be attributed to several factors. First, higher concentrations result in increased competition among dye molecules for active catalytic sites, leading to site saturation and a reduction in available reaction sites. Additionally, higher dye concentrations may limit light penetration due to excessive absorption by the dye itself, thereby reducing the photocatalyst's activation efficiency. Moreover, the number of photogenerated reactive species, such as superoxide radicals $(\bullet O_2^-)$ and holes (h^+) , may not be sufficient to degrade all RhB molecules effectively at high concentrations, leading to a slower degradation rate.

The adsorption phase, observed before light irradiation (t < 0), showed a notable decrease in RhB concentration, indicating significant dye adsorption onto the photocatalyst in dark conditions. The extent of adsorption was higher at lower initial concentrations, likely due to the greater availability of active sites for dye molecules to bind. Upon light irradiation, the photocatalytic degradation initiated, and the removal efficiency was highest for the lowest initial concentrations. This behavior suggests that at lower concentrations, RhB molecules have better interaction with reactive species, and there is minimal interference from excess dye molecules. In contrast, at higher concentrations, catalyst site saturation and increased recombination of photogenerated charge carriers limit degradation efficiency. To improve degradation at higher RhB concentrations, strategies such as increasing catalyst dosage to provide more active sites and enhancing light intensity or reaction time could be considered.

3.5. Adsorption isotherm and kinetic studies

The reaction behavior between the equilibrium solution concentration C_e (mg/L) and the equilibrium adsorption capacity q_e (mg/g) at constant temperature could be analyzed by adsorption isotherm. This allows you to determine how RhB interacts with the catalyst surface before photocatalysis starts. To evaluate the adsorption behavior of RhB in the darkness onto PVP-assisted UiO-66(Ce), Langmuir and Freundlich isotherms were analyzed. These models provide insights into the adsorption capacity, surface homogeneity, and interaction mechanism between the adsorbate and adsorbent. The experimental data were fitted to the Langmuir and Freundlich isotherm models and plotted in Fig. S3. The Langmuir model assumes monolayer adsorption on a homogeneous surface, whereas the Freundlich model describes multilayer adsorption on heterogeneous surfaces. The linearized equations are given as follows [53]:

Table 2Comparison of photocatalytic rate constants of RhB over different photocatalysts.

Photocatalyst	Rate constant (k) (1/min)	Light source	Ref.
ZnO	0.0128	UV	[56]
70 % Pb ₃ Nb ₄ O ₁₃ /fumed SiO ₂	0.059	Visible	[57]
$FeO + H_2O_2$	0.0038	UV	[58]
0.5 wt%MoS ₂ /Bi ₂ O ₂ CO ₃	0.0298	UV	[59]
C and N Codoped TiO ₂	0.0427	Visible	[54]
Fly ash-based-inorganic polymer	0.01051	UV	[60]
TiO ₂ QD-Kaolinite	0.0151	Sunlight	[61]
1 wt% PANI@CoTiO ₃	0.0173	UV	[62]
0.1 PVP/CAN UiO-6(Ce)	0.0207	Visible	This work

Langmuir Isotherm:

$$\frac{C_e}{q_e} = \frac{1}{K_L Q_m} + \frac{C_e}{Q_m} \tag{2}$$

where C_e is equilibrium concentration of adsorbate, q_e is the amount of adsorbate adsorbed per unit mass of adsorbent, Q_m is the maximum adsorption capacity, and K_L is Langmuir constant.

Freundlich Isotherm:

$$log q_e = log K_F + \frac{1}{n} log C_e \tag{3}$$

where K_F and n are Freundlich constants indicating adsorption capacity and intensity, respectively.

As shown in Table S3, the Langmuir model yielded a maximum adsorption capacity (Q_m) of 303.03 mg/g, whereas the Freundlich constant (K_F) was 3.65 mg/g, with an adsorption intensity (n) of 1.22. The Freundlich model exhibited a better fit $(R^2=0.9921)$ compared to the Langmuir model $(R^2=0.9356)$, indicating that adsorption occurs on a heterogeneous surface with multilayer adsorption. The adsorption is heterogeneous, meaning different adsorption sites have varying affinities for the adsorbate.

To study the photodegradation kinetics of RhB, Langmuir-Hinshelwood (L-H) model was applied which is the pseudo-first-order kinetic one

$$Ln\frac{C_t}{C_0} = -kt \tag{4}$$

where k is the rate constant of photocatalysis, C_0 is the initial RhB concentration, and C_t is RhB concentration at time t.

According to the calculations (Fig. S3), the rate constant is $k=0.0207\ 1/\text{min}$ which indicates moderate photocatalytic activity for RhB degradation compared to some catalysts, such as C and N Codoped TiO_2 which show higher rate constants, suggesting faster degradation rates [54] (Table 2).

3.6. Mechanism study

3.6.1. Scavengers test

As shown in Fig. 7a, the introduction of SO significantly suppresses the photodegradation activity of the photocatalyst and reduces the efficiency from 80 % to 25 %, demonstrating the photogenerated holes play a crucial role in the photocatalytic reaction. The addition of BQ also decreases the photocatalytic activity and reduces the efficiency from 80 % to 10 %, showing that \bullet O²⁻ is also a major activated species. However, methanol has almost no effect on photodegradation, manifesting that \bullet OH almost has no effect on photodegradation of RhB and is not responsible for the degradation.

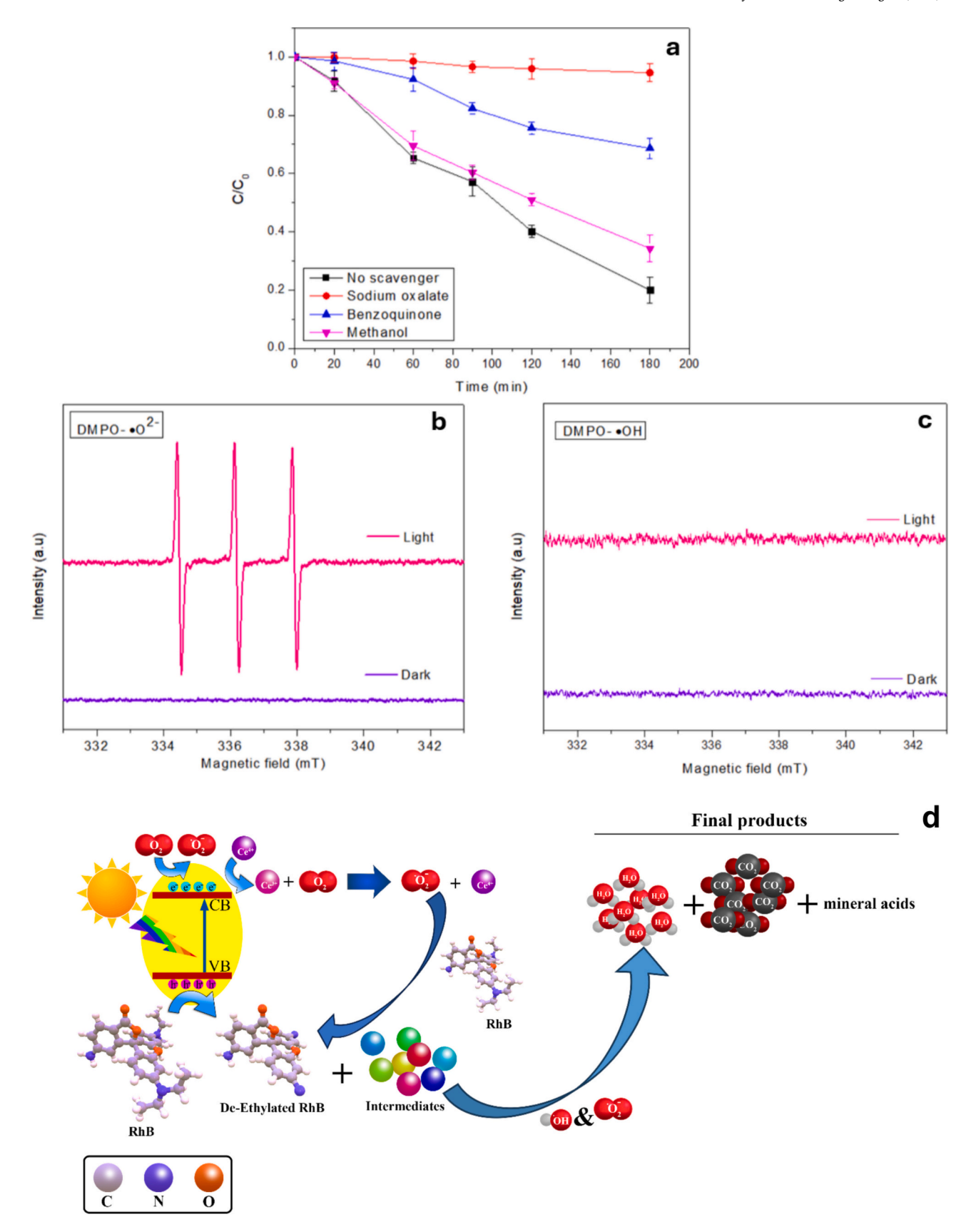


Fig. 7. Identification of active species in the visible-light photodegradation of RhB over 0.1 wt% PVP-assisted UiO-66(Ce): (a) effects of specific scavengers (trapping experiments); (b) EPR spectra of DMPO-trapped superoxide radicals (\bullet O² $^-$); (c) EPR spectra of DMPO-trapped hydroxyl radicals (\bullet OH), and (d) Proposed mechanism for the photodegradation of RhB over PVP-assisted UiO-66(Ce).

3.6.2. EPR analysis

To further confirm the involvement of catalyst species $\bullet O^2$ in the light catalytic reaction during the catalytic degradation process, an EPR experiment was conducted using DMPO as a capture agent for \bullet O²⁻ and •OH. As shown in Fig. 7b and c, no characteristic peak of DMPO-•O² was observed under dark conditions, while the peak of $\bullet O^2$ became evident after being exposed to visible light. However, no characteristic peak of DMPO-•OH was detected, which further supports that •O² - is a crucial active species involved in photodegradation processes consistent with capture experiments [26]. Combining the results of the radical trapping experiment and the EPR analysis, we propose a plausible photocatalytic mechanism for the 0.1 wt% PVP-assisted UiO-66(Ce) photocatalyst under light irradiation. When exposed to light with energy equal to or greater than the bandgap energy, electrons in the valence band (VB) of the 0.1 wt% PVP-assisted UiO-66(Ce) photocatalyst are excited and transition to the conduction band (CB), leading to the formation of electron-hole pairs. The CB of 0.1 wt% PVP-assisted UiO-66 (Ce) (-1.1 eV) is positioned at a more negative potential than the redox potential of $O_2/\bullet O_2^-$ (-0.33 eV), allowing the photogenerated electrons in the CB to efficiently reduce dissolved molecular oxygen (O2) to superoxide radicals $(\bullet O_2^-)$ in addition to the oxygen species within the MOF structure, as shown in the EPR spectrum (Fig. 7b). The significant signal for DMPO-•O₂ observed under light irradiation confirms that superoxide radicals are the primary reactive species driving the photocatalytic degradation process. In the absence of light, no signal for superoxide was detected, further validating that the radical formation is light dependent.

In contrast, the trapping experiment with isopropanol (IPA) for hydroxyl radicals (•OH) yielded no significant signal in the EPR analysis (Fig. 7c), indicating that hydroxyl radicals are not actively involved in the photocatalytic degradation process. This is consistent with the radical trapping experiment, where the addition of IPA did not affect the degradation efficiency, suggesting that •OH radicals are not the main contributors to the photodegradation in this system.

The band structure of UiO-66 (Ce) plays a crucial role in the formation of reactive oxygen species. The VB of 0.1 wt% PVP-assisted UiO-66 (Ce) (+1.79 eV) is positioned below the potential needed for $\rm H_2O/\bullet OH$ formation (+2.40 eV), meaning that the photogenerated holes in the VB cannot oxidize $\rm H_2O$ to generate $\bullet OH$ radicals. Therefore, the superoxide radicals ($\bullet O_2^-$), generated from the reduction of oxygen molecules are the predominant active species and from the MOF structure, particularly through $\rm Ce^{4+}/\rm Ce^{3+}$ cycling and defect sites, as confirmed by the EPR and radical trapping experiments. This mechanism highlights the importance of the 0.1 wt% PVP-assisted UiO-66 (Ce)'s band structure in selectively generating reactive species that contribute to the enhanced photocatalytic performance.

3.6.3. Proposed mechanism and possible intermediates

Regarding scavenger test and EPR analysis, the mechanism can be described as follows. When the photocatalyst is exposed to visible light, electrons (e⁻) in the VB are excited to the CB, leaving behind holes (h⁺) in the VB.

$$PVP-assisted~UiO-66(Ce)+\textit{h}\nu~(visible~light) \rightarrow e^{-}~(CB)+h^{+}~(VB)$$

This activation initiates the photocatalytic process, where the excited electrons in the CB can subsequently interact with dissolved oxygen (O₂), leading to the formation of superoxide radicals (\bullet O₂). In addition to dissolved oxygen, the oxygen species within the MOF structure, particularly through Ce^{4+/}Ce³⁺ redox cycling and defect sites, also contribute to the generation of \bullet O₂. These reactive species, along with the generated holes, play a crucial role in the degradation pathways of Rhodamine B.

$$\begin{array}{l} e^{-}\left(CB\right)+O_{2}\rightarrow\bullet O_{2}^{-}\\ \left\{\begin{array}{ll} Ce^{4+}+e^{-}\rightarrow Ce^{3+} & \left(ReductionofCe^{4+}toCe^{3+}\right)\\ Ce^{3+}+O_{2}\rightarrow Ce^{4+}+\bullet O_{2}^{-} & \left(Interaction with oxygen mole\right) \end{array}\right.$$

Initially, N-deethylation occurs as the $\bullet O_2^-$ radicals and h^+ attack the ethyl groups (RhB contains four ethyl (-C₂H₅) groups attached to its amine structure) on the RhB molecule, resulting in the stepwise removal of these groups, producing N-deethylated intermediates (the loss of ethyl groups changes the color and electronic structure of RhB, contributing to its degradation). Following this, the breakdown of the conjugated chromophore structure takes place, leading to the decolorization of RhB.

$$RhB + \bullet O_2^-/h^+ \rightarrow N - deethylated RhB + intermediates$$

Finally, the intermediate products undergo further oxidation, ultimately transforming into inorganic end products such as carbon dioxide (CO₂), water (H₂O), and mineral acids, completing the photocatalytic degradation process.

Degraded intermediates \rightarrow CO₂ + H₂O + mineral acids

In studies employing GC–MS for Rhodamine B degradation, various intermediates have been identified. For instance, a study utilizing a system of $\rm Bi_2WO_6$ detected intermediates such as benzoic acid, phthalic acid, terephthalic acid, and succinic acid [55]. A schematic diagram of the proposed mechanism is shown on Fig. 7d.

3.7. Stability and reusability

To evaluate the reusability of the synthesized photocatalysts, three consecutive degradation cycles were conducted, each lasting 150 min, based on prior experiments. After each cycle, the catalyst was recovered by centrifugation and dried at 60 $^{\circ}$ C overnight. It is worth noting that no washing or recovery process was performed on the photocatalysts between cycles, indicating their intrinsic stability and reusability under continuous operation. As illustrated in Fig. S4, the removal efficiency of RhB exhibited a slight decline of about 3.4 $^{\circ}$ 6 in degradation efficiency across all cycles. These results suggest that the PVP-assisted UiO-66(Ce) composite maintains stability and remains effective over three cycles.

Further analysis was performed to assess changes in the structural integrity of the recovered PVP-assisted UiO-66(Ce) nanoparticles. The ICP-OES analysis was employed to investigate the potential leaching of Ce metal ions from the PVP-assisted UiO-66(Ce) into the solution. Results indicated that only a minimal amount (<0.2 wt%) of this metal was released, which could explain the slight reduction in catalytic efficiency over successive cycles.

As depicted in Fig. S5, the FTIR spectra of the regenerated photocatalyst exhibit overall similar band positions to those of the fresh sample, indicating the structural integrity of the MOF framework was preserved throughout the photocatalytic cycles. Minor changes, however, were observed in band intensities, particularly at 1643 cm⁻¹ and 1374 cm⁻¹, corresponding to the C≡O stretching in carboxylic acid and the symmetric O-C-O stretching of the carboxylate group in the BDC ligand, respectively [33]. The attenuation of these peaks suggests partial removal of surface-bound PVP and BDC ligands, likely due to repeated washing or photodegradation under reaction conditions. Additionally, the disappearance or weakening of small peaks in the 800-1277 cm-1 region-assigned to O-H and C-H bending in the BDC ligand and C-N stretching vibrations associated with PVP-further supports this hypothesis. These variations may also arise from surface contamination, or the adsorption of intermediate by-products not fully removed during postreaction cleaning. The observed spectral differences are thus attributed to surface-level modifications rather than framework decomposition, consistent with the preserved XRD patterns. Overall, the data confirms the chemical stability and reusability of the MOF-based photocatalyst.

Furthermore, XPS of the fresh photocatalyst was compared to the

Table 3Summary of RhB photodegradation efficiency of various photocatalysts.

Photocatalyst	Degradation efficiency (%)	Band gap (eV)	Irradiation/ lamp power (W)	RhB concentration (mg/l)	Contact time (min)	Catalyst dosage (g/L)	Ref.
Boron-Doped g-C ₃ N ₄	98	2.7	Visible/300	4	40	2	[63]
Bi ₂₅ FeO ₄₀ -rGO	~90	1.65	Visible/500	20	240	0.4	[64]
C,N-codoped TiO ₂	94	2.9	Visible/36	20	90	1.8	[54]
Bi ₂ WO ₆ loaded N-biochar	99	2.28	Visible/100	10	45	1	[65]
Bi ₂ O ₃ @LDHs	90	1.93	Visible/400	50	180	0.4	[66]
Pd/ZrO ₂	~70	_	None (H ₂ O ₂ alone)	15	300	0.05	[67]
g-C ₃ N ₄	95	2.66	Sunlight	24	320	0.3	[68]
ZnO/NCQD nanorods	90	2.7	UV/70	~5	30	0.2	[69]
LaFeO ₃ -MoS ₂	96	2.14	Visible/500	12	150	0.8	[70]
Fe/MgO-rGO	86	2.78	Visible/500	15	240	0.8	[71]
BiFeO ₃ /hg-C ₃ N ₄	~100	2.25	Visible/300	10	60	0.5	[72]
Ag@Cr ₂ O ₃ NPs	97.5	_	Sunlight	5	60	0.8	[73]
BiOCl@COF-1	90	3.08	Visible/500	20	50	0.1	[74]
PANI@NiTiO ₃	94	2.63	Visible/50	5	180	1	[62]
0.1 PVP/CAN UiO-66(Ce)	93	2.2	Visible/150	10	150	0.06	This work

used one. Since this is photocatalytic removal, there is no RhB on the catalysts due to the degradation by light. The comparison of Ce 3d XPS spectra of fresh and spent 0.1 PVP UiO-66 (Ce) is shown in Fig. S6. It can be clearly seen from the plot that the Ce $^{4+}$ peak around 886 eV has reduced significantly in the spent 0.1 PVP UiO-66 (Ce) after the photocatalysis along with the increase in intensity of the Ce $^{3+}$ peak. This could be one of the reasons for the possible lower catalytic activity of the spent catalyst.

4. Comparison with other photocatalysts

In order to investigate the highest dye removal efficiency of the photocatalyst, an additional experiment was carried out at the optimum condition (the optimum pH was maintained at 7, a catalyst dosage of 0.2 g/L of catalyst was used, the photodegradation lasted for 150 min, the experiment was conducted at room temperature, and the initial dye concentration was set at 10 mg/L) and the average value, with less than 10 % variation, with findings reported in the literature from the last five years. Regarding the effect of initial RhB concentration and catalyst dosage on the time required for near-complete degradation, the results showed that the synthesized MOF in the present study is comparable to or better than many reported systems that required higher dosages (e.g., 1.8 g/L [48]) or longer contact times (e.g., 320 min [54]) for the selected dye, which makes it a strong candidate for the removal of dye contaminated wastewater (Table 3).

5. Conclusions

This study successfully demonstrated the synthesis of UiO-66(Ce) via metal substitution using cerium salt and its effective application as a photocatalyst for the degradation of Rhodamine B (RhB). The resulting nanocrystals exhibited a high surface area $(1340 \text{ m}^2/\text{g})$, an average pore diameter of 1.64 nm, and a band gap of 2.6 eV, enabling visible-lightdriven photocatalysis. The introduction of PVP as a capping agent significantly improved photocatalytic performance by reducing particle aggregation and size. Among the synthesized samples, the optimal 0.1 wt% PVP/CAN ratio led to a reduced band gap of 2.2 eV and a notable decrease in particle size from 400 nm to 110 nm. UV-Vis analysis confirmed enhanced adsorption and photocatalytic activity with PVP assistance, while recycling experiments showed that the catalyst retained its activity for at least three cycles. The kinetics of adsorption in the dark, as well as the photocatalytic degradation under light, were investigated. The adsorption data were best described by the Freundlich isotherm, while the photocatalytic process followed the Langmuir-Hinshelwood model, with a rate constant of 0.0207 1/min. Mechanistic insights from trapping experiments and EPR analysis identified

photogenerated holes (h⁺) and superoxide radicals (\bullet O₂) as the dominant reactive species, whereas hydroxyl radicals (\bullet OH) played a minor role. A removal efficiency of 92.9 \pm 0.4 % was achieved when 0.06 g/L of the catalyst was applied to a 10 mg/L RhB solution over 150 min. This performance is comparable to, or even better than, many previously reported systems requiring higher catalyst dosages or longer reaction times. The results demonstrate that UiO-66(Ce) nanomaterials exhibit significant potential for the photodegradation of organic pollutants, particularly for wastewater treatment under visible-light conditions.

CRediT authorship contribution statement

Maliheh Heravi: Writing – original draft, Visualization, Formal analysis, Data curation, Conceptualization. Ali Ahmadpour: Writing – review & editing, Supervision, Project administration, Investigation, Funding acquisition. Tahereh Rohani Bastami: Writing – review & editing, Supervision, Methodology, Investigation. Mika Sillanpää: Writing – review & editing, Investigation, Funding acquisition.

Declaration of competing interest

The authors declare that they have no known competing financial interests or personal relationships that could have appeared to influence the work reported in this paper.

Acknowledgment

The authors gratefully acknowledge Ferdowsi University of Mashhad, Iran (Grant No. 46023), and Lappeenranta University of Technology (LUT), Finland, for providing laboratory facilities and support during the experimental work.

Appendix A. Supplementary data

Supplementary data to this article can be found online at https://doi.org/10.1016/j.jwpe.2025.108615.

Data availability

Data will be made available on request.

References

[1] B.C. Chen, W.H. Liao, C.C. Wu, High-stability CsPbIBr₂ nanocrystal with nitrogen-doped graphene quantum dot/titanium dioxide for enhancing rhodamine B photocatalytic degradation under visible light, J. Environ. Chem. Eng. 10 (2022) 107534, https://doi.org/10.1016/j.jece.2022.107534.

- [2] A.U. Khan, M. Zahoor, M.U. Rehman, A.B. Shah, I. Zekker, F.A. Khan, R. Ullah, G. M. Albadrani, R. Bayram, H.R.H. Mohamed, Biological mineralization of methyl orange by Pseudomonas aeruginosa, Water (Switzerland) 14 (2022), https://doi.org/10.3390/w14101551.
- [3] V. Zeynali, S.M. Mousavi, E. Saljoughi, S. Kiani, M. Sillanpää, Chitosan/polyvinyl alcohol/hydroxyapatite nanocomposite membrane for the efficient adsorption of Congo red anionic dye, Polym. Compos. 44 (2023) 4227–4242, https://doi.org/10.1002/pc.27393.
- [4] S. Sudarshan, V.S. Bharti, S. Harikrishnan, S.P. Shukla, G. RathiBhuvaneswari, Ecotoxicological effect of a commercial dye Rhodamine B on freshwater microalgae Chlorella vulgaris, Arch. Microbiol. 204 (2022) 1–16, https://doi.org/10.1007/s00203-022-03254-5.
- [5] Y. Zhao, Y. Shi, H. Yang, M. Liu, L. Shen, S. Zhang, Y. Liu, J. Zhu, J. Lan, J. Li, S. Ge, Stem cell microencapsulation maintains stemness in inflammatory microenvironment, Int. J. Oral Sci. 14 (2022), https://doi.org/10.1038/s41368-022-00198-w
- [6] C. Liu, H. Liu, J.C. Yu, L. Wu, Z. Li, Strategies to engineer metal-organic frameworks for efficient photocatalysis, Chin. J. Catal. 55 (2023) 1–19, https://doi. org/10.1016/S1872-2067(23)64556-5.
- [7] D. Chen, Y.T. Zheng, N.Y. Huang, Q. Xu, Metal-organic framework composites for photocatalysis, EnergyChem 6 (2024) 100115, https://doi.org/10.1016/j. enchem.2023.100115.
- [8] I. Ahmad, Y. Zou, J. Yan, Y. Liu, S. Shukrullah, M.Y. Naz, H. Hussain, W.Q. Khan, N.R. Khalid, Semiconductor photocatalysts: a critical review highlighting the various strategies to boost the photocatalytic performances for diverse applications, Adv. Colloid Interf. Sci. 311 (2023) 102830, https://doi.org/ 10.1016/j.cis.2022.102830
- [9] M. Pourmadadi, M.M. Eshaghi, S. Ostovar, A. Shamsabadipour, S. Safakhah, M. S. Mousavi, A. Rahdar, S. Pandey, UiO-66 metal-organic framework nanoparticles as gifted MOFs to the biomedical application: a comprehensive review, J. Drug Deliv. Sci. Technol. 76 (2022) 103758, https://doi.org/10.1016/j.iddx/2022/103758
- [10] M. Treger, A. Hannebauer, A. Schaate, J.L. Budde, P. Behrens, A.M. Schneider, Tuning the optical properties of the metal-organic framework UiO-66 via ligand functionalization, Phys. Chem. Chem. Phys. 25 (2023) 6333–6341, https://doi. org/10.1039/d2cp03746g.
- [11] D. Zou, D. Liu, Understanding the modifications and applications of highly stable porous frameworks via UiO-66, Mater. Today Chem. 12 (2019) 139–165, https://doi.org/10.1016/i.mtchem.2018.12.004.
- [12] A.S. Yasin, J. Li, N. Wu, T. Musho, Study of the inorganic substitution in a functionalized UiO-66 metal-organic framework, Phys. Chem. Chem. Phys. 18 (2016) 12748–12754, https://doi.org/10.1039/c5cp08070c.
- [13] A. Dhakshinamoorthy, A. Santiago-Portillo, A.M. Asiri, H. Garcia, Engineering UiO-66 metal organic framework for heterogeneous catalysis, ChemCatChem 11 (2019) 899–923, https://doi.org/10.1002/cctc.201801452.
- [14] K. Gayathri, K. Vinothkumar, Y.N. Teja, B.M. Al-shehri, M. Selvaraj, Ligand-mediated band structure engineering and physiochemical properties of UiO-66 (Zr) metal-organic frameworks (MOFs) for solar-driven degradation of dye molecules, Colloids Surf. A Physicochem. Eng. Asp. 653 (2022) 1–12.
 [15] X.P. Wu, L. Gagliardi, D.G. Truhlar, Cerium metal-organic framework for
- [15] X.P. Wu, L. Gagliardi, D.G. Truhlar, Cerium metal-organic framework for photocatalysis, J. Am. Chem. Soc. 140 (2018) 7904–7912, https://doi.org/ 10.1021/jacs.8b03613.
- [16] D. Zhao, C. Cai, Cerium-based UiO-66 metal-organic framework for synergistic dye adsorption and photodegradation: a discussion of the mechanism, Dyes Pigments 185 (2021) 108957, https://doi.org/10.1016/j.dyepig.2020.108957.
- [17] V. Mahmoodi, A. Ahmadpour, T.R. Bastami, M.T.H. Mosavian, PVP assisted synthesis of high efficient BiOI/graphene oxide nanohybrid and its photocatalytic performance in degradation of organic dye pollutants, Sol. Energy 176 (2018) 483–495, https://doi.org/10.1016/j.solener.2018.10.056.
- [18] M. Kurakula, G.S.N.K. Rao, Pharmaceutical assessment of polyvinylpyrrolidone (PVP): as excipient from conventional to controlled delivery systems with a spotlight on COVID-19 inhibition, J. Drug Deliv. Sci. Technol. 60 (2020) 102046, https://doi.org/10.1016/j.iddst.2020.102046.
- [19] I.A. Safo, M. Werheid, C. Dosche, M. Oezaslan, The role of polyvinylpyrrolidone (PVP) as a capping and structure-directing agent in the formation of Pt nanocubes, Nanoscale Adv. 1 (2019) 3095–3106, https://doi.org/10.1039/c9na00186g.
- [20] Z.B. Shifrina, V.G. Matveeva, L.M. Bronstein, Role of polymer structures in catalysis by transition metal and metal oxide nanoparticle composites, Chem. Rev. 120 (2020) 1350–1396, https://doi.org/10.1021/acs.chemrev.9b00137.
- [21] J. He, S. Razzaque, S. Jin, I. Hussain, B. Tan, Efficient synthesis of ultrafine gold nanoparticles with tunable sizes in a hyper-cross-linked polymer for nitrophenol reduction, ACS Appl. Nano Mater. 2 (2019) 546–553, https://doi.org/10.1021/ acsanm.8b02112.
- [22] A. Bayat, M. Shakourian-Fard, N. Talebloo, M.M. Hashemi, Silver nanoparticles immobilized onto poly(4-vinylpyridine)-functionalized magnetic nanoparticles: a robust magnetically recyclable catalyst for oxidant-free alcohol dehydrogenation, Appl. Organomet. Chem. 32 (2018) 16–20, https://doi.org/10.1002/aoc.4061.
- [23] B. Şen, A. Aygün, A. Şavk, S. Duman, M.H. Calimli, E. Bulut, F. Şen, Polymer-graphene hybrid stabilized ruthenium nanocatalysts for the dimethylamine-borane dehydrogenation at ambient conditions, J. Mol. Liq. 279 (2019) 578–583, https://doi.org/10.1016/j.molliq.2019.02.003.
- [24] M. Lammert, M.T. Wharmby, S. Smolders, B. Bueken, A. Lieb, K.A. Lomachenko, D. De Vos, N. Stock, Cerium-based metal organic frameworks with UiO-66 architecture: synthesis, properties and redox catalytic activity, Chem. Commun. 51 (2015) 12578–12581, https://doi.org/10.1039/c5cc02606g.

- [25] M. Heravi, V. Srivastava, A. Ahmadpour, V. Zeynali, M. Sillanpää, The effect of the number of -SO³⁻ groups on the adsorption of anionic dyes by the synthesized hydroxyapatite/Mg-Al LDH nanocomposite, Environ. Sci. Pollut. Res. 31 (2024) 17426–17447, https://doi.org/10.1007/s11356-024-32192-6.
- [26] M. Zhang, M. Xing, B. Dong, X. Sun, H. Zhang, C. Wang, H. Zhu, Constructing a type-II heterojunction of AgI/CO₃²-Bi₂O₂CO₃ for enhanced photocatalytic degradation of organic pollutants, Mater. Chem. Phys. 318 (2024) 129274, https://doi.org/10.1016/j.matchemphys.2024.129274.
- [27] E. Omrani, A. Ahmadpour, M. Heravi, T.R. Bastami, Novel ZnTi LDH/h-BN nanocomposites for removal of two different organic contaminants: simultaneous visible light photodegradation of Amaranth and Diazepam, J Water Process Eng 47 (2022), https://doi.org/10.1016/j.jwpe.2022.102581.
- [28] M.J. Kalmutzki, N. Hanikel, O.M. Yaghi, Secondary building units as the turning point in the development of the reticular chemistry of MOFs, Sci. Adv. 4 (2018), https://doi.org/10.1126/sciady.aat9180.
- [29] Y. Cao, Y. Zhao, Z. Lv, F. Song, Q. Zhong, Preparation and enhanced CO₂ adsorption capacity of UiO-66/graphene oxide composites, J. Ind. Eng. Chem. 27 (2015) 102–107, https://doi.org/10.1016/j.jiec.2014.12.021.
- [30] B. Mirhosseini-Eshkevari, M. Esnaashari, M.A. Ghasemzadeh, Novel Brönsted acidic ionic liquids confined in UiO-66 nanocages for the synthesis of dihydropyrido[2,3-d]pyrimidine derivatives under solvent-free conditions, ACS Omega 4 (2019) 10548–10557, https://doi.org/10.1021/acsomega.9b00178.
- [31] Y. Li, Y. Zhao, R. Zhang, G. Lu, SO₃, Inorg. Chem. Commun. 82 (2017) 68–71, https://doi.org/10.1016/j.inoche.2017.05.021.
- [32] H. Fotovat, M. Khajeh, A.R. Oveisi, M. Ghaffari-Moghaddam, S. Daliran, A hybrid material composed of an amino-functionalized zirconium-based metal-organic framework and a urea-based porous organic polymer as an efficient sorbent for extraction of uranium(VI), Microchim. Acta 185 (2018), https://doi.org/10.1007/ s00604-018-2991-3.
- [33] H.G. Kim, K. Choi, K. Lee, S. Lee, K.W. Jung, J.W. Choi, Controlling the structural robustness of zirconium-based metal organic frameworks for efficient adsorption on tetracycline antibiotics, Water (Switzerland) 13 (2021), https://doi.org/ 10.3390/w13131869.
- [34] M. Davarpanah, A. Ahmadpour, T. Rohani-Bastami, H. Dabir, Synthesis and application of diethanolamine-functionalized polystyrene as a new sorbent for the removal of p-toluenesulfonic acid from aqueous solution, J. Ind. Eng. Chem. 30 (2015) 281–288, https://doi.org/10.1016/j.jiec.2015.05.034.
- [35] M. Davarpanah, A. Ahmadpour, T. Rohani Bastami, Preparation and characterization of anion exchange resin decorated with magnetite nanoparticles for removal of p-toluic acid from aqueous solution, J. Magn. Magn. Mater. 375 (2015) 177–183, https://doi.org/10.1016/j.jmmm.2014.09.065.
- [36] Z. Zhang, B. Tan, L. Xie, Z. Han, H. Quan, D. Chen, Electrochemically tailoring oxygen functionalities and pores in ordered mesoporous carbon for enhanced H₂O₂ production, Appl. Catal. B Environ. 379 (2025) 125703, https://doi.org/10.1016/ i.apcatb.2025.125703.
- [37] D. González, C. Pazo-carballo, E. Camú, Y. Hidalgo-rosa, X. Zarate, N. Escalona, E. Schott, Adsorption Properties of M-UiO-66 (M = Zr(IV); Hf(IV) or Ce(IV)) with BDC or PDC Linker, 2024, pp. 10486–10498, https://doi.org/10.1039/ d4df00941i.
- [38] Y. Wang, C. Yang, C. Zhang, M. Duan, H. Wang, H. Fan, Y. Li, J. Shangguan, J. Lin, Effect of hierarchical porous MOF-199 regulated by PVP on their ambient desulfurization performance, Fuel 319 (2022) 123845, https://doi.org/10.1016/j. firel_2022_123845
- [39] R. Muruganantham, Y.J. Gu, Y. Da Song, C.W. Kung, W.R. Liu, Ce-MOF derived ceria: insights into the Na-ion storage mechanism as a high-rate performance anode material, Appl. Mater. Today 22 (2021) 100935, https://doi.org/10.1016/j. apmt.2021.100935.
- [40] Q. Gong, T. Gao, H. Huang, R. Wang, P. Cao, G. Zhou, Double-shelled CeO₂@C hollow nanospheres as enhanced anode materials for lithium-ion batteries, Inorg. Chem. Front. 5 (2018) 3197–3204, https://doi.org/10.1039/c8qi01068d.
- [41] X. Chen, E. Yu, S. Cai, E. Yu, H. Jia, S. Cai, P. Liang, J. Chen, J. Chen, In situ pyrolysis of Ce-MOF to prepare CeO₂ catalyst with obviously improved catalytic performance for toluene combustion, Chem. Eng. J. 344 (2018) 469–479, https://doi.org/10.1016/j.cej.2018.03.091.
- [42] J. He, Y. Xu, W. Wang, B. Hu, Z. Wang, X. Yang, Y. Wang, L. Yang, Ce(III) nanocomposites by partial thermal decomposition of Ce-MOF for effective phosphate adsorption in a wide pH range, Chem. Eng. J. 379 (2020), https://doi. org/10.1016/j.cej.2019.122431.
- [43] Z. Zhang, H. Shi, Q. Wu, X. Bu, Y. Yang, J. Zhang, Y. Huang, MOF-derived CeO₂/ Au@SiO₂ hollow nanotubes and their catalytic activity toward 4-nitrophenol reduction, New J. Chem. 43 (2019) 4581–4589, https://doi.org/10.1039/ c8ni05745a
- [44] O. Merka, V. Yarovyi, D.W. Bahnemann, M. Wark, pH-control of the Photocatalytic Degradation Mechanism of Rhodamine B Over Pb₃Nb₄O₁₃, 2011, pp. 8014–8023.
- [45] D.H. Han, H. Park, T. Goto, S. Cho, Y. Seo, Y. Kondo, H. Nishida, T. Sekino, Effects of Cation Exchange in Rhodamine B Photocatalytic Degradation Using Peroxo-Titanate Nanotubes, 2024, pp. 1–15.
- [46] F. Zhang, Z. Sun, B. Yan, Z. Cao, H. Li, G.L. Jing, X. Liu, Degradation of Rhodamine B by CuFe₂O₄ nanoparticles anchored on montmorillonite as an activator of sodium persulfate, J. Taiwan Inst. Chem. Eng. 150 (2023) 105073, https://doi.org/ 10.1016/j.jtice.2023.105073.
- [47] A.A. Al-Kahtani, Photocatalytic degradation of rhodamine B dye in wastewater using gelatin/CuS/PVA nanocomposites under solar light irradiation, J. Biomater. Nanobiotechnol. 08 (2017) 66–82, https://doi.org/10.4236/jbnb.2017.81005.

- [48] A. Ahmad, X. Meng, N. Yun, Z. Zhang, Preparation of hierarchical BiOBr microspheres for visible light-induced photocatalytic detoxification and disinfection 2016 (2016), https://doi.org/10.1155/2016/1373725.
- [49] S. Abuzerr, M. Darwish, A.H. Mahvi, Simultaneous removal of cationic methylene blue and anionic reactive red 198 dyes using magnetic activated carbon nanoparticles: equilibrium, and kinetics analysis, Water Sci. Technol. 2017 (2017) 534–545, https://doi.org/10.2166/wst.2018.145.
- [50] E. Rápó, S. Tonk, Factors affecting synthetic dye adsorption; desorption studies: a review of results from the last five years (2017–2021), Molecules 26 (2021), https://doi.org/10.3390/molecules26175419.
- [51] R.G.D. Kishore, Investigation of photocatalytic degradation of rhodamine B by using nanosized TiO2, Int. J. Sci. Res. Manage. 5 (2017) 6006–6013, https://doi. org/10.18535/ijsrm/v5i7.25
- [52] Y. Guo, C. Zhou, L. Fang, Z. Liu, W. Li, M. Yang, Effect of pH on the catalytic degradation of rhodamine B by synthesized CDs/g-C₃N₄/Cu xO composites, ACS Omega 6 (2021) 8119–8130, https://doi.org/10.1021/acsomega.0c05915.
- [53] M. Zahoor, A. Ullah, S. Alam, M. Muhammad, R.H. Setyobudi, I. Zekker, A. Sohail, Novel magnetite nanocomposites (Fe₃O₄/C) for efficient immobilization of ciprofloxacin from aqueous solutions through adsorption pretreatment and membrane processes, Water (Switzerland) 14 (2022), https://doi.org/10.3390/ w14050724
- [54] T.T.T. Le, T.D. Tran, Photocatalytic degradation of rhodamine B by C and N codoped TiO₂ nanoparticles under visible-light irradiation, J. Chemother. 2020 (2020), https://doi.org/10.1155/2020/4310513.
- [55] Z. He, C. Sun, S. Yang, Y. Ding, H. He, Z. Wang, Photocatalytic degradation of rhodamine B by Bi₂WO₆ with electron accepting agent under microwave irradiation: mechanism and pathway, J. Hazard. Mater. 162 (2009) 1477–1486, https://doi.org/10.1016/j.jhazmat.2008.06.047.
- [56] D. Yu, R. Cai, Z. Liu, Studies on the photodegradation of Rhodamine dyes on nanometer-sized zinc oxide 60 (2004) 1617–1624, https://doi.org/10.1016/j. saa.2003.09.003.
- [57] X. Li, J. Ye, Photocatalytic Degradation of Rhodamine B Over Pb₃Nb₄O₁₃/Fumed SiO₂ Composite Under Visible Light Irradiation, 2007, pp. 13109–13116.
- [58] A. Mehrdad, B. Massoumi, R. Hashemzadeh, Kinetic study of degradation of Rhodamine B in the presence of hydrogen peroxide and some metal oxide, Chem. Eng. J. 168 (2011) 1073–1078, https://doi.org/10.1016/j.cej.2011.01.087.
- [59] Q. Wang, G. Yun, Y. Bai, N. An, J. Lian, H. Huang, B. Su, Photodegradation of rhodamine B with MoS₂/Bi₂O₂CO₃ composites under UV light irradiation, Appl. Surf. Sci. 313 (2014) 537–544, https://doi.org/10.1016/j.apsusc.2014.06.018.
- [60] O.K. Kabbaj, M. Taibi, Synergetic influence between adsorption and photodegradation of Rhodamine B using synthesized fly ash based inorganic polymer 24 (2021). https://doi.org/10.1016/j.surfin.2021.101136.
- [61] M.E. Awad, A.M. Farrag, A.A. El-Bindary, M.A. El-Bindary, H.A. Kiwaan, C, Appl. Organomet. Chem. 37 (2023) 1–17, https://doi.org/10.1002/aoc.7113.
- [62] M. Abouri, A. Benzaouak, M. Elouardi, L. El Hamdaoui, F. Zaaboul, K. Azzaoui, B. Hammouti, R. Sabbahi, S. Jodeh, M.A. El Belghiti, A. El Hamidi, Enhanced

- photocatalytic degradation of Rhodamine B using polyaniline-coated XTiO₃(X=Co, Ni) nanocomposites, Sci. Rep. 15 (2025) 3595, https://doi.org/10.1038/s41598-024-83610-1.
- [63] S.C. Yan, Z.S. Li, Z.G. Zou, Photodegradation of Rhodamine B and Methyl Orange over boron-doped g-C₃N₄ under visible light irradiation 26 (2010) 3894–3901, https://doi.org/10.1021/la904023j.
- [64] M.A. Basith, R. Ahsan, I. Zarin, M.A. Jalil, Enhanced photocatalytic dye degradation and hydrogen production ability of Bi₂₅FeO₄₀-rGO nanocomposite and mechanism insight, Sci. Rep. 8 (2018) 33–35, https://doi.org/10.1038/s41598-018-29402-w.
- [65] T. Wang, S. Liu, W. Mao, Y. Bai, K. Chiang, K. Shah, J. Paz-Ferreiro, Novel Bi₂WO⁶ loaded N-biochar composites with enhanced photocatalytic degradation of rhodamine B and Cr(VI), J. Hazard. Mater. 389 (2020) 121827, https://doi.org/10.1016/j.jhazmat.2019.121827.
- [66] L. Zhang, Y. Meng, H. Shen, J. Li, C. Yang, B. Xie, S. Xia, Applied surface science photocatalytic degradation of rhodamine B by Bi₂O₃ @ LDHs S – scheme heterojunction: performance, kinetics and mechanism, Appl. Surf. Sci. 567 (2021) 150760, https://doi.org/10.1016/j.apsusc.2021.150760.
- [67] S. Jabeen, M.S. Khan, R. Khattak, I. Zekker, J. Burlakovs, S.S. Rubin, M. M. Ghangrekar, A. Kallistova, N. Pimenov, M. Zahoor, G.S. Khan, Palladium-supported zirconia-based catalytic degradation of, Water 13 (2021) 1–13.
- [68] A.A. Yadav, S.W. Kang, Y.M. Hunge, Photocatalytic degradation of Rhodamine B using graphitic carbon nitride photocatalyst, J. Mater. Sci. Mater. Electron. 32 (2021) 15577–15585, https://doi.org/10.1007/s10854-021-06106-y.
- [69] S.K. Mandal, S. Paul, S. Datta, D. Jana, Nitrogenated CQD decorated ZnO nanorods towards rapid photodegradation of rhodamine B: a combined experimental and theoretical approach, Appl. Surf. Sci. 563 (2021) 150315, https://doi.org/ 10.1016/j.apsusc.2021.150315.
- [70] S. Das, S. Dutta, A.M. Tama, M.A. Basith, Nanostructured LaFeO₃-MoS₂ for efficient photodegradation and photocatalytic hydrogen evolution, Mater. Sci. Eng. B 271 (2021), https://doi.org/10.1016/j.mseb.2021.115295.
- [71] F. Sharmin, D. Chandra Roy, M.A. Basith, Photocatalytic water splitting ability of Fe/MgO-rGO nanocomposites towards hydrogen evolution, Int. J. Hydrog. Energy 46 (2021) 38232–38246, https://doi.org/10.1016/j.ijhydene.2021.09.072.
- [72] H. Cui, Z. Wang, G. Cao, Y. Wu, J. Song, Y. Li, L. Zhang, J. Mu, X. Chou, Facilitated photocatalytic degradation of rhodamine B over one-step synthesized honeycomb-like BiFeO3/g-C₃N₄ catalyst, Nanomaterials 12 (2022) 1–18, https://doi.org/10.3390/nano12223970.
- [73] L.S. Alqarni, M.D. Alghamdi, A.A. Alshahrani, N.F. Alotaibi, S.M.N. Moustafa, K. Ashammari, I.A. Alruwaili, A.M. Nassar, C, Nanomaterials 14 (2024), https://doi.org/10.3390/nano14030289.
- [74] D. Ma, J. Tang, G. He, Y. Xue, S. Pan, F. Liu, J. Zhao, Enhancing photocatalytic degradation of rhodamine B with visible-light-driven HCl-assisted Bi₂O₃ photocatalysts: activity, mechanism, and pathways, Mater. Sci. Semicond. Process. 181 (2024) 108672, https://doi.org/10.1016/j.mssp.2024.108672.